CHALMERS
UNIVERSITY OF TECHNOLOGY

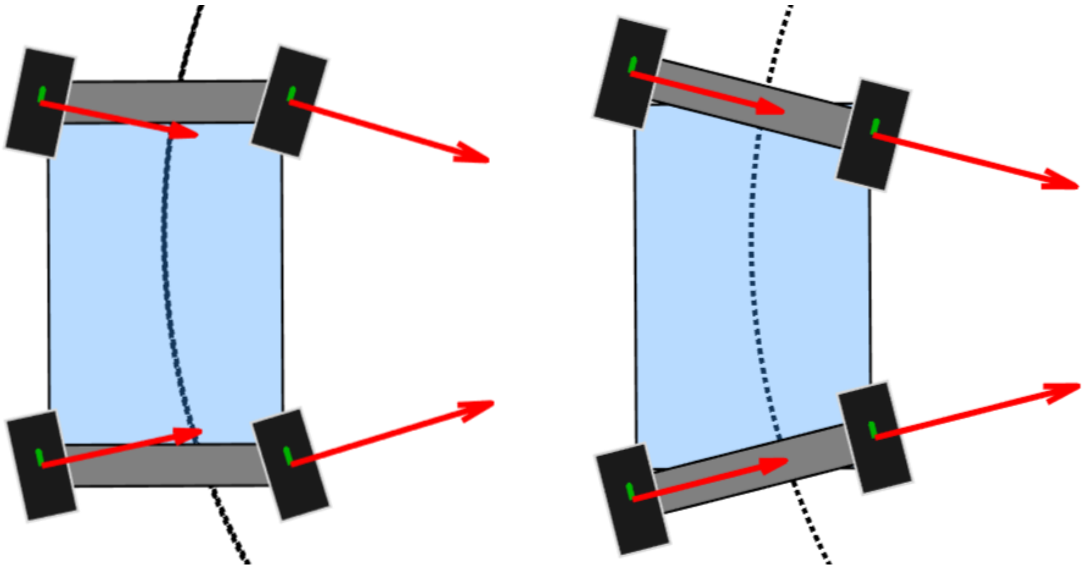

Control Strategies for Reducing Ground Tear in Agricultural Vehicles with Over-actuated Steering

Master's thesis in Systems, Control and Mechatronics

Johan Ewaldsson

Gustaf Ivarsson

DEPARTMENT OF MECHANICS AND MARITIME SCIENCES

CHALMERS UNIVERSITY OF TECHNOLOGY

Gothenburg, Sweden 2026

www.chalmers.se

Master's Thesis in Systems, Control and Mechatronics

Control Strategies for Reducing Ground Tear in Agricultural Vehicles with Overactuated Steering

A Comparative Study of LQR, MPC, and PI Control for Tire and Pivot Steering Mechanisms

Johan Ewaldsson
Gustaf Ivarsson

CHALMERS
UNIVERSITY OF TECHNOLOGY

Department of Mechanics and Maritime Sciences
Division of Systems and Control
Chalmers University of Technology
Gothenburg, Sweden 2026

Control Strategies for Reducing Ground Tear in Agricultural Vehicles with Overactuated Steering
A Comparative Study of LQR, MPC, and PI Control for Tire and Pivot Steering Mechanisms
Johan Ewaldsson
Gustaf Ivarsson

© Johan Ewaldsson, Gustaf Ivarsson, 2026.

Supervisor: Andreas Käck, QRTECH
Examiner: Fredrik Bruzelius, Mechanical Engineering

Master's Thesis 2026
Department of Mechanics and Maritime Sciences
Chalmers University of Technology
SE-412 96 Gothenburg
Sweden
Telephone +46 31 772 1000

Cover: Visualization of the tire steering and pivot steering model simulation during a turn.

Typeset in LaTeX
Gothenburg, Sweden 2026

Control Strategies for Reducing Ground Tear in Agricultural Vehicles with Overactuated Steering
A Comparative Study of LQR, MPC, and PI Control for Tire and Pivot Steering Mechanisms
Johan Ewaldsson
Gustaf Ivarsson
Department of Mechanics and Maritime Sciences
Division of Systems and Control
Chalmers University of Technology

Abstract

This thesis investigates how two different steering configurations, tire steering and pivot steering, as well as control strategies can be utilized to reduce ground impact caused by shear forces in different scenarios. The vehicle dynamics for the two steering configurations and their ground interaction on deformable soil is modelled and simulated using Matlab. A state space formulation for each steering setup is derived and used for the development of an LQR and MPC controller. The control objective is reference tracking of the longitudinal velocity, and front and rear steering angles with the ultimate goal of reducing excessive shear forces. The developed model-based controllers utilize input rate penalties to promote smooth control actions, as well as weighting terms on slip ratio and slip angle, which are directly related to the generated shear forces. In addition, the MPC formulation incorporates explicit constraints, allowing tire slip to be directly limited. A PI controller is also developed as a benchmark for comparison with the model-based controllers.

Both the steering configurations and developed controllers are evaluated in simulation under both uniform and asymmetric terrain conditions. The pivot steering model combined with the implemented controller shows a reduction in total shear force compared to the tire steering model. However, it shows slightly reduced capabilities in reference tracking performance compared to tire steering. The model based controllers were successfully implemented and shows improved performance compared with the PI controller in terms of ground impact reduction as a result of the input rate limitations. Furthermore, the model based controllers could successfully incorporate slip ratio weights for reduction of longitudinal shear forces. The MPC also provided promising results in incorporating weights on slip angle and direct constraints on tire slip. Both steering configurations successfully incorporates an extended Kalman filter for state estimation, although with reduced performance.

Keywords: LQR, MPC, Slip reduction, Pivot steering, EKF, Model based control, Ground shear stress

Acknowledgements

We would like to give a special thanks to our supervisor Andreas Käck at QRTECH for supporting us throughout the duration of this thesis work. He has been helpful with guidance as well as insight into the field.

We also thank QRTECH for allowing us to carry out this thesis at their location and providing us with resources, expert support and good company.

Lastly, we thank our examiner at Chalmers, Fredrik Bruzelius at the department of mechanical engineering for support during the writing of this thesis.

Johan Ewaldsson, Gustaf Ivarsson, Gothenburg, June 2026

List of Acronyms

Below is the list of acronyms that have been used throughout this thesis listed in alphabetical order:

EKF	Extended Kalman Filter
LQR	Linear Quadratic Regulator
MPC	Model Predictive Control
PI	Proportional - Integral
RMSE	Root Mean Square Error
IMU	Inertial Measurement Unit

Nomenclature

Below is the nomenclature of indices, parameters, and variables that have been used throughout this thesis.

Indices

$i = 1$	Front left tire
$i = 2$	Front right tire
$i = 3$	Rear left tire
$i = 4$	Rear right tire
$i_a = 1$	Front axis
$i_a = 2$	Rear axis
k	Discrete time step index
t	Continuos time

Parameters

r	Tire radius
m	Mass at each tire
M	Total vehicle mass
I_t	Tire moment of inertia
I_v	Vehicle moment of inertia
I_a	Axle moment of inertia
$L_{x,i}$	Longitudinal distance to tire from vehicle centre of mass
$L_{y,i}$	Lateral distance to tire from vehicle centre of mass
l_{x,i_a}	Longitudinal distance to axle mid point from vehicle centre of mass
$l_{y,i}$	Lateral distance to tire from axle mid point

K	Shear deformation modulus
k_c	Cohesive pressure sinkage module
k_ϕ	Frictional pressure sinkage module
n	Sinkage exponent
c	Soil cohesion
j	Shear displacement
ϕ	Internal friction angle
σ	Normal stress
ρ	Soil density
Λ	Wheel sinkage coefficient
h	Tire sinkage
h_s	Tire static sinkage
θ_s	Tire static contact angle
θ_f	Tire entry angle
θ_r	Tire exit angle
B	Bulldozing resistance
T_c	Steering time constant

Variables

$v_{x,cm}^v$	Longitudinal velocity at vehicle's centre of mass in vehicle coordinates
$v_{y,cm}^v$	Lateral velocity at vehicle's centre of mass in vehicle coordinates
$v_{x,i}^v$	Longitudinal velocity at tire in vehicle coordinates
$v_{y,i}^v$	Lateral velocity at tire in vehicle coordinates
$v_{x,i}^t$	Longitudinal velocity at tire in tire coordinates
$v_{y,i}^t$	Lateral velocity at tire in tire coordinates
$F_{x,i}^v$	Longitudinal tire force in vehicle coordinates
$F_{y,i}^v$	Lateral tire force in vehicle coordinates
$F_{x,i}^t$	Longitudinal tire force in tire coordinates
$F_{y,i}^t$	Lateral tire force in tire coordinates
ω_i	Angular velocity for tire
T_i	Applied torque for tire
λ_i	Tire slip ratio

β_i	Tire slip angle
$\tau_{x,i}$	Longitudinal tire shear stress
$\tau_{y,i}$	Lateral tire shear stress
δ_F	Front steering angle
δ_R	Rear steering angle
ψ	Vehicle yaw angle
$\dot{\psi}$	Vehicle yaw rate

Contents

List of Figures

List of Tables

1 Introduction

1.1 Background

Modern agriculture relies on a variety of heavy vehicles for daily tasks such as field work and transportation. Although these vehicles are necessary for many agricultural tasks, their interaction with the ground can cause unwanted effects such as soil compaction and surface tear damage. The latter is caused by shear forces between the tires of the vehicle and the ground. The reduction of ground damage is especially desirable in fields and on sensitive roads where vehicles continuously use the same transportation route. High shear forces can arise when there is excessive relative motion between the tires and the ground, both longitudinally due to wheel slip and laterally due to slip angle, where the wheel heading differs from its actual direction of motion. Therefore, there is an interest in vehicle steering and control strategies that reduce these forces while also maintaining sufficient tracking performance to handle the heavy tasks.

A possible tool for reducing the ground impact lies in how the vehicle's steering is realized. Vehicles equipped with distributed drive, such as hub-mounted wheel motors, provide additional control authority since the driving torque at each wheel can be regulated independently. This enables a more flexible distribution of tire forces during manoeuvring. Furthermore, vehicles with over-actuated steering possess more inputs than strictly required to realize a desired vehicle motion, which also creates possibilities for optimizing the turning command to reduce peaks in shear forces. Instead of using one fixed steering motion to achieve a desired yaw rate, the available actuators can be coordinated so that the required tire forces are distributed more evenly between the wheels. This can reduce local peaks in slip ratio and slip angle, which are closely related to the shear forces acting on the ground. Therefore, over-actuated steering and distributed drive systems provide a promising basis for control strategies aimed at reducing ground damage while maintaining vehicle manoeuvrability.

At Flivab, an electric assistance vehicle for agricultural applications is currently being developed in collaboration with QRTECH. The vehicle has distributed electric drive and is over actuated with independent yaw rotation for the front and rear axles. The steering works by controlling the velocities of the different tires. This setup creates opportunities for innovative steering algorithms and can be utilized in order to reduce the ground impact. The current implementation uses a PI controller for the realisation of the steering and movement. While this setup works, it may not be optimal for reducing the generated shear forces. Other control methods are therefore of interest. This thesis focuses on modelling the vehicle for simulation as well as analysing model based control strategies with the aim of reducing ground impact while maintaining reference tracking capabilities. A Linear Quadratic Regulator (LQR) as well as Model Predictive Controller (MPC) is investigated together with an implemented PI controller used for comparison. The controlled outputs are the velocity as well as the steering on the front and rear axle. The model based controllers allows for additional control authority where slip may be considered directly in the control objective. The developed pivot steering method will also be analysed and compared with a more traditional tire steering model from a ground impact perspective. The two types of steering configurations are visualized in Figures 1.1a and 1.1b.

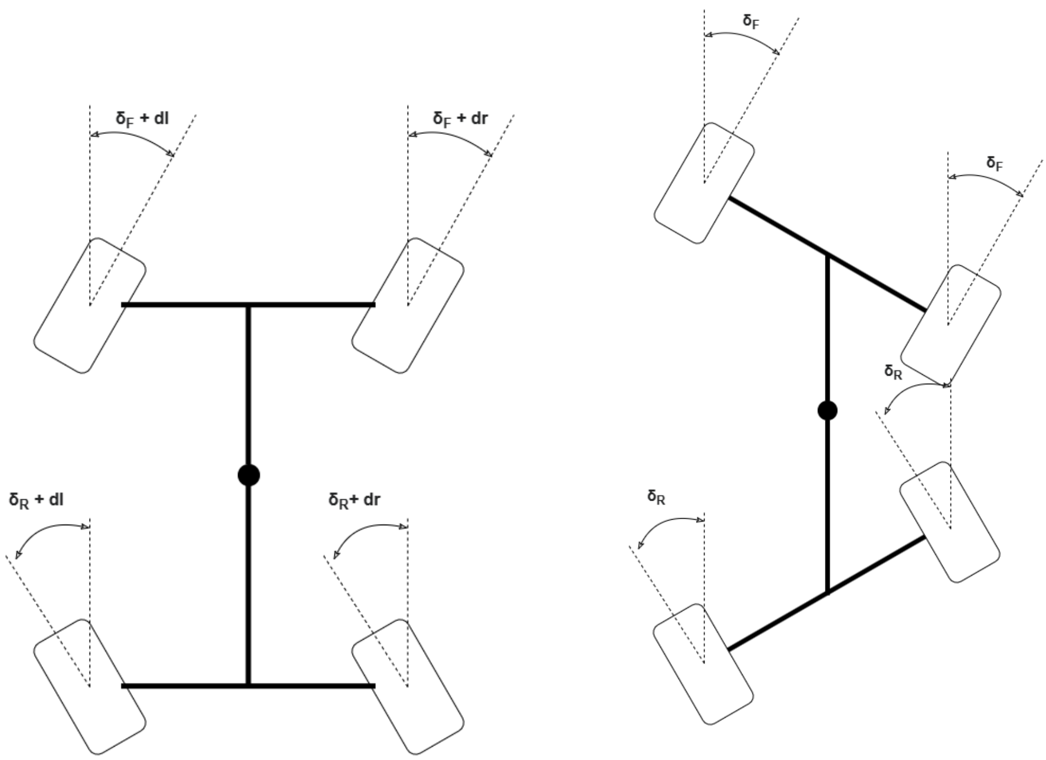

(a) Tire steering. **(b)** Pivot steering.

Figure 1.1: Visualization of tire steering and pivot steering.

1.2 Purpose

The purpose of this report is to analyse how the tire and pivot steering configurations described in Figures 1.1a and 1.1b differ in terms of generated shear forces. Two model based controllers, an LQR and MPC, are developed and compared with a PI controller for both of the steering implementations. For the developed controllers, reference tracking and slip reduction capabilities are investigated and compared with the implemented PI controller.

1.3 Research Questions

This thesis aims to answer the following research questions:

- How do tire steering and pivot steering differ in terms of generated shear forces during manoeuvring?
- Can model-based controllers such as LQR and MPC reduce excessive slip and shear forces compared to the existing PI controller?
- How does reducing slip affect the reference tracking performance of the vehicle?
- How robust are the different steering configurations and controllers when the ground conditions change?

1.4 Limitations

In order to narrow down the project and make it feasible within the time-frame, the following limitations are set:

- The project will only analyse shear forces along the ground surface and not ground impact related to the sinkage.
- The simulations will only be conducted on even terrain without slopes.
- The ground type and corresponding coefficients will be assumed to be known and not estimated for use in tire modelling and controller tuning. Different ground types with known parameters will be investigated.
- Performance results will be based merely on simulations.

2
Theory

This chapter presents the theory used for the project. It is divided into two sections, the first of which covers theory related to vehicle and tire dynamics that was used for developing the simulation models for the tire and pivot steering vehicles. The second section defines relevant theory and definitions related to control theory that were used as basis for the model based controller implementation.

2.1 Tire Dynamics

This section describes the theory for tire-ground interaction on deformable terrain that is used in the vehicle simulations.

2.1.1 Tire Slip

Following [1], the slip ratio and slip angle are defined as

$$\lambda = \frac{r\omega - v_x}{\max(r\omega, v_x)} \tag{2.1}$$

and

$$\beta = -\arctan\left(\frac{v_y}{v_x}\right), \tag{2.2}$$

respectively. Here, r is the tire radius, ω is the tire angular velocity, and v_x and v_y are the longitudinal and lateral velocities of the tire center in the tire-fixed coordinate frame, see Figure 2.1. The slip ratio describes the longitudinal slippage between the tire and the ground and is bounded to the interval [-1,1]. A value of $\lambda = 0$ corresponds to pure rolling, while $\lambda > 0$ indicates tractive slip, where $r\omega > v_x$, and $\lambda < 0$ indicates braking slip, where $r\omega < v_x$. The slip angle describes the difference between the direction in which the tire is pointing and the actual direction of motion of the tire.

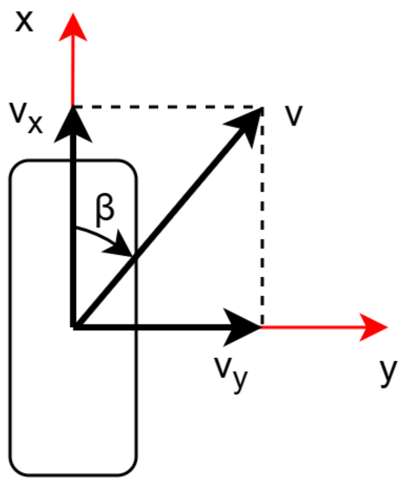

Figure 2.1: Slip angle for the tire.

The slip ratio λ and slip angle β of a tire are directly related to the longitudinal and lateral tire forces, as described further below.

2.1.2 Wheel Sinkage

The wheel sinkage model used in this section follows the terramechanics formulation presented in [1]. On deformable terrain, a tire will sink a certain amount. The sinkage of a moving tire can be divided into two parts: static sinkage, that depends on the vehicle's vertical load and dynamic sinkage, that arises from the tire rotation. The static sinkage can be determined from Bekker's pressure–sinkage relationship for a flat plate with sinkage h and width b as

$$p(h) = (k_c/b + k_\phi)h^n \tag{2.3}$$

where $p(h)$ is pressure, k_c and k_ϕ represent ground specific pressure-sinkage modules and n is the sinkage exponent. The wheel sinkage at an arbitrary wheel angle θ is given by

$$h(\theta) = r(\cos\theta - \cos\theta_s) \tag{2.4}$$

where θ_s is the static contact angle. Substituting equation 2.4 into equation 2.3 gives

$$p(\theta) = r^n(k_c/b + k_\phi)(\cos\theta - \cos\theta_s)^n. \tag{2.5}$$

The static contact angle is found from vertical force equilibrium. For a given value of θ_s, the pressure distribution over the contact patch is known from the previous equations. The correct value of θ_s is therefore the one for which the integrated vertical terrain reaction equals the applied wheel load W:

$$W = \int_{-\theta_s}^{\theta_s} p(\theta) br\cos\theta d\theta = r^{n+1}(k_c + k_\phi b)\int_{-\theta_s}^{\theta_s}(\cos\theta - \cos\theta_s)^n\cos\theta d\theta. \tag{2.6}$$

This equation does not give θ_s explicitly, since θ_s appears both in the integration limits and inside the integrand. Therefore, θ_s is obtained numerically by varying θ_s

until the right-hand side of the equation matches the known wheel load W. The static sinkage, h_s, is then determined as

$$h_s = r(1 - \cos\theta_s) \tag{2.7}$$

and is visualized in Figure 2.2. The dynamic sinkage is a function of wheel surface patterns, soil characteristics, and slip ratio and is neglected in this report for simplicity.

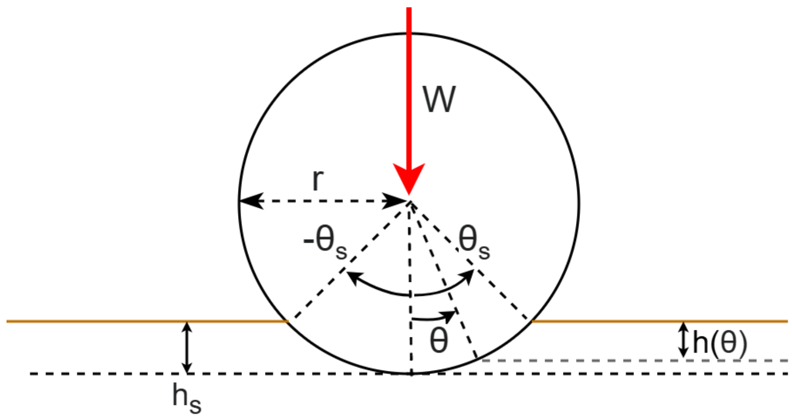

Figure 2.2: Static contact angle and static sinkage for a tire.

2.1.3 Wheel Contact Angles

The entry angle θ_f of a tire on deformable soil is defined as the angle from the vertical to where the tire makes contact with the soil. Similarly, the exit angle θ_r is defined as the angle from the vertical to where the wheel departs from the soil. These can be expressed as functions of the sinkage h as

$$\theta_f = \cos^{-1}(1 - h/r) \tag{2.8}$$

$$\theta_r = \cos^{-1}(1 - \Lambda h/r) \tag{2.9}$$

where Λ is the wheel sinkage ratio. The value of Λ depends on soil characteristics, tire patterns, and slip ratio. A value of $\Lambda < 1$ indicates soil compaction behind the tire, whereas $\Lambda > 1$ indicates that soil is dug up by the wheel and transported backwards. The wheel angles used in the model are illustrated in Figure 2.3. A tire's contact patch on deformable soil is defined by the region between θ_f and θ_r.

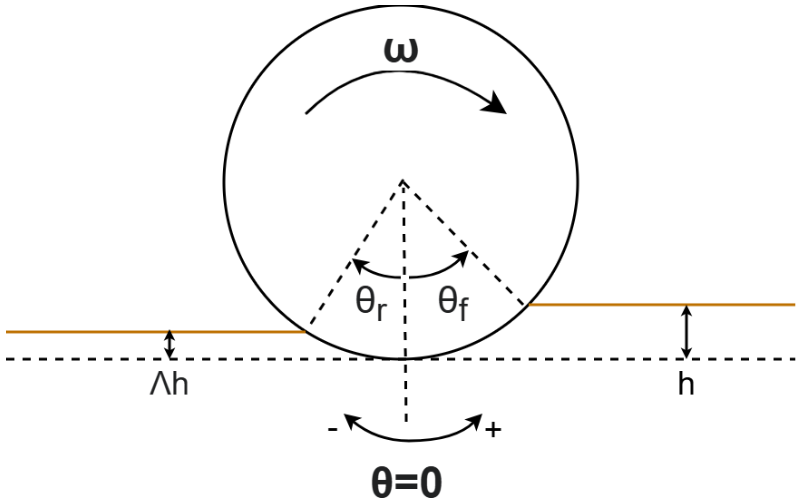

Figure 2.3: Wheel contact angles θ_f and θ_r. For this case, $\Lambda < 1$.

2.1.4 Stress Distribution

The stresses beneath a rotating wheel consist of normal stresses, acting perpendicular to the wheel–soil contact surface, and shear stresses, acting tangentially along the contact interface. Following [2], the normal stress at a given angle θ can be determined as

$$\sigma(\theta) = \begin{cases} r^n \left(\frac{k_c}{b} + k_\phi\right) (\cos(\theta) - \cos(\theta_f))^n & \theta_m \leq \theta < \theta_f \\ r^n \left(\frac{k_c}{b} + k_\phi\right) \left(\cos\left(\theta_f - \frac{\theta-\theta_r}{\theta_m-\theta_r}(\theta_f - \theta_m)\right) - \cos(\theta_f)\right)^n & \theta_r \leq \theta < \theta_m \end{cases} \tag{2.10}$$

where θ_m is the angle at which the normal stress is maximized. This angle is defined as

$$\theta_m = (a_0 + a_1\lambda)\theta_f, \tag{2.11}$$

where a_0 and a_1 are parameters that depend on the interaction between the wheel and the soil. The values are generally assumed as $a_0 \approx 0.4$ and $0 \leq a_1 \leq 0.3$.
The soil shear stress at a given angle θ under a tire is determined using the Janosi-Hanamoto formula as described in [3], given by

$$\tau(\theta) = \tau_{\max}(\theta)\left(1 - e^{-j(\theta)/K}\right), \tag{2.12}$$

where $j(\theta)$ is the shear displacement and K is the shear deformation modulus. The maximum shear strength of the soil is expressed as [3]

$$\tau_{\max}(\theta) = c + \sigma(\theta)\tan(\phi), \tag{2.13}$$

where c denotes the soil cohesion and ϕ is the internal friction angle of the soil.
In the tire-fixed coordinate frame, the longitudinal shear displacement is defined according to [3] as

$$j_x(\theta) = r\left(\theta_f - \theta - (1-\lambda)(\sin(\theta_f) - \sin(\theta))\right), \tag{2.14}$$

while the lateral shear displacement is defined according to [4] as

$$j_y(\theta) = r(1-\lambda)(\theta_f - \theta)\tan(\beta). \tag{2.15}$$

2.1.5 Tire Forces

The resulting longitudinal force of the tire can be determined by integrating the shear stress $\tau_x(\theta)$ and longitudinal component of the normal stress $\sigma(\theta)$ over the contact patch according to [3] as

$$F_x = rb\int_{\theta_r}^{\theta_f} \tau_x(\theta)\cos(\theta) - \sigma(\theta)\sin(\theta)d\theta \tag{2.16}$$

The lateral tire force has two components

$$F_y = F_u + F_s$$

where F_u represents the force developed by $\tau_y(\theta)$ and F_s is the force generated by the bulldozing phenomenon on the side face of the tire [4]. The total force can be calculated by integrating the two components over the contact patch as

$$F_y = \int_{\theta_r}^{\theta_f} \underbrace{rb\tau_y(\theta)}_{F_u} + \underbrace{B(r - h(\theta)\cos(\theta))d\theta}_{F_s} \tag{2.17}$$

where B is the bulldozing resistance [5], which can be expressed as

$$B = \frac{1}{2}\rho h(\theta)^2 \tan^2\left(\frac{\pi}{4} + \frac{\phi}{2}\right) + 2h(\theta)c\tan\left(\frac{\pi}{4} + \frac{\phi}{2}\right) \tag{2.18}$$

where ρ is the soil density.

2.2 Model Based Control

This section defines the base for the theory used for developing the model based controllers.

2.2.1 Discretization

A system with states, x, whose dynamics can be described by a set of first order equations with known inputs, can be written in state space form as

$$\dot{x} = Ax(t) + Bu(t)$$
$$y = Cx(t) + D(u(t)$$

where u is the input and y describes the output of the system. The continuous time state space model can be discretized using the using the matrix exponential method. For a sampling time T_s the discrete time matrices given by [6]

$$A_d = e^{ATs} \tag{2.19}$$

$$B_d = \int_0^{Ts} e^{A\tau} B d\tau \tag{2.20}$$

where Ts is the sampling time and A_d and B_d represents the discretised matrices of A and B. The discretized state space then becomes

$$\begin{aligned} x(k+1) &= A_d x(k) + B_d u(k) \\ y(k) &= Cx(k) + Du(k) \end{aligned} \tag{2.21}$$

2.2.2 Linearization

A non linear system can be describe in the state space form as

$$\dot{x} = F(x,u)$$

$$y = G(x,u)$$

where $F(x,u)$ and $G(x,u)$ are nonlinear function of the states and inputs. In order to use linear control method is it necessary to linearize these models around an operating point. This is done with a first order Taylor expansion of F and G, evaluated at a desired state x_0 and input u_0. The deviation variables are defined as

$$\Delta x = x - x_0$$

$$\Delta u = u - u_0$$

The linearized state space model can then be written as the deviation from the operating point

$$\Delta \dot{x} = A\Delta x + B\Delta u,$$

$$\Delta y = C\Delta x + D\Delta u$$

where the system matrices are given by [7]

$$A = \left.\frac{\partial F(x,u)}{\partial x}\right|_{x_0,u_0}, \qquad B = \left.\frac{\partial F(x,u)}{\partial u}\right|_{x_0,u_0}. \tag{2.22}$$

$$C = \left.\frac{\partial G(x,u)}{\partial x}\right|_{x_0,u_0}, \qquad D = \left.\frac{\partial G(x,u)}{\partial u}\right|_{x_0,u_0}. \tag{2.23}$$

This only approximates the states close to the linearized point.

2.2.3 LQR

Linear Quadratic Regulator (LQR) control is a model based control strategy that minimizes a quadratic cost function that considers state error against control effort. For discrete time, the cost function is defined as [8]

$$J = \sum_{k=0}^{\infty} (x(k)^T Q x(k) + u(k)^T R u(k)) \tag{2.24}$$

With the solution to the discrete algebraic riccati equation

$$P = A^T P A - (A^T P B)(R + B^T P B)^{-1}(B^T P A) + Q \tag{2.25}$$

the optimal discrete gain is determined as

$$K = (R + B^T P B)^{-1} B^T P A \tag{2.26}$$

The controller law is therefore

$$u(k) = -K x(k) \tag{2.27}$$

2.2.4 MPC

Model predictive control (MPC) is a model based control strategy that works by predicting future system behaviour to compute an optimal sequence of control actions. At each time step, a finite-horizon constrained optimization problem is solved using a system model. The objective is to minimize a cost function that penalizes tracking errors and control effort. Only the first control input is applied to the system and the optimization is repeated at the next time step using updated measurements. The optimization can be formulated in terms of the system outputs where future outputs are predicted over a prediction horizon N_p, while the control inputs are optimized over a control horizon $N_c \leq N_p$. Constraints on both inputs and outputs can be included explicitly. The optimization problem can be defined as

$$\begin{aligned}
\min_{\{u_k\}} \quad & \sum_{k=1}^{N_p} (y(k) - r(k))^T Q_y (y(k) - r(k)) + \sum_{k=0}^{N_c - 1} u(k)^T R u(k) \\
\text{s.t.} \quad & x(k+1) = A x(k) + B u(k), \quad k = 0, \ldots, N_p - 1 \\
& y(k) = C x(k) + D u(k), \quad k = 1, \ldots, N_p \\
& u_{\min} \leq u(k) \leq u_{\max}, \quad k = 0, \ldots, N_c - 1 \\
& y_{\min} \leq y(k) \leq y_{\max}, \quad k = 1, \ldots, N_p \\
& u(k) = u(N_c - 1), \quad k = N_c, \ldots, N_p - 1
\end{aligned} \tag{2.28}$$

with $x(0)$ given[9]. Here, Q_y and R are weighting matrices that balance tracking performance and control effort.

2.2.5 Extended Kalman Filter

In many systems, not all states in a state space can be measured directly. This may be due to physical limitations or that the system is not equipped with the relevant sensors. Furthermore, sensor measurements are often affected by noise, which can reduce the accuracy. For this reason, state estimation is often necessary to estimate unmeasured states or increase accuracy in the measured states. For nonlinear systems, an Extended Kalman Filter (EKF) can be used. The EKF extends the standard Kalman filter by using a non-linear process and measurement model. The process model describes how the states evolve over time while the measurement model describes the expected sensor values. Since the standard Kalman filter assumes a linear model, the EKF linearizes the nonlinear model around the current operating point [10].

The EKF recursion used in this work is given by [10]. The system is described by

$$x(k) = f(x(k-1), u(k-1) + w(k-1))$$

$$z(k) = h(x(k) + v(k))$$

where $f(\cdot)$ is the nonlinear process model, $h(\cdot)$ is the measurement mode, $w(k)$, $v(k)$ are the process respectively measurement noise. Both the process and measurement noise is assumed to be zero mean with the covariance matrixes $Q(k)$ and $R(k)$. The prediction is initially computed with the nonlinear process model

$$\tilde{x}(k) = f(\hat{x}(k-1), u(k-1))$$

with the predicted covariance as

$$\tilde{P}(k) = A(k)P(k-1)A(k)^T + Q(k).$$

The Kalman gain is then computed as

$$K(k) = \tilde{P}(k)H(k)^T(H(k)\tilde{P}(k)H(k)^T + R(k))^{-1}. \tag{2.29}$$

The prediction is then updated using the Kalman gain along with the difference in sensor measurement and the measurement model

$$\hat{x}(k) = \tilde{x}(k) + K(k)(y_{meas}(k) - h(\tilde{x}(k))).$$

Finally, the covariance is updated

$$P(k) = (I - K(k)H(k)\tilde{P}(k)).$$

3

Methods

3.1 Modelling

The vehicle modelling was done in Simulink with Simscape components using the equations defined in this section. A separate model was made for tire steering and pivot steering but with a similar structure except for a few differences which follows from the difference in tire position relative to the centre of mass, described further below.

3.1.1 Tire Forces Modelling

Assuming that the wheel's entry angle θ_f and exit angle θ_r, defined in 2.1.3, are known, the integrals in Equations 2.16 and 2.17 can be estimated using three points along the tire contact patch, θ_f, θ_r and the mid point $\theta_{mid} = (\theta_f + \theta_r)/2$. Given the tire velocities $v_{x,i}^t$ and $v_{y,i}^t$ and the tire's angular velocity ω_i, the slip ratio λ and slip angle β can be determined using Equations 2.1 and 2.2. The lateral and longitudinal shear displacement can be calculated at each of the three points using Equations 2.14 and 2.15. The total shear displacement is then determined as

$$j(\theta_q) = \sqrt{j_x(\theta_q)^2 + j_y(\theta_q)^2} \tag{3.1}$$

where $q \in \{f, \mathrm{mid}, r\}$. The total shear stress is calculated using equation **??** as

$$\tau(\theta_q) = \tau_{max}(\theta_q)(1 - e^{-j(\theta_q)/K}) \tag{3.2}$$

where

$$\tau_{max}(\theta_q) = (c + \sigma(\theta_q)\tan(\phi)) \tag{3.3}$$

and $\sigma(\theta_j)$ is determined for each point using Equation 2.10. The lateral and longitudinal shear stresses are then determined as

$$\tau_x(\theta_q) = \tau(\theta_q)\left(\frac{j_x(\theta_q)}{j(\theta_q)}\right) \tag{3.4}$$

and

$$\tau_y(\theta_q) = \tau(\theta_q)\left(\frac{j_y(\theta_q)}{j(\theta_q)}\right). \tag{3.5}$$

The integrand of the integrals in Equations 2.16 and 2.17 is evaluated for each point, according to

$$f_{x,q} = \tau_x(\theta_q)\cos\theta_q - \sigma(\theta_q)\sin\theta_q \tag{3.6}$$

and

$$f_{y,q} = rb\tau_y(\theta_q) + R_b(r - h(\theta_q)\cos\theta_q). \tag{3.7}$$

Simpson's 1/3 rule [11] is then applied, resulting in the approximate longitudinal and lateral tire forces

$$F^t_{x,i} = rb\frac{d\theta}{6}\left(f_{x,f} + 4f_{x,mid} + f_{x,r}\right) \tag{3.8}$$

and

$$F^t_{y,i} = \frac{d\theta}{6}\left(f_{y,f} + 4f_{y,mid} + f_{y,r}\right) \tag{3.9}$$

where $d\theta = \theta_f - \theta_r$.

3.1.2 Tire Steering Vehicle Modelling

For the tire steering model, the forces $F^t_{x,i}$ and $F^t_{y,i}$ are transformed from the tire fixed coordinate system to the vehicle fixed coordinate system as

$$\begin{bmatrix} F^v_{x,i} \\ F^v_{y,i} \end{bmatrix} = \begin{bmatrix} \cos\delta_i & -\sin\delta_i \\ \sin\delta_i & \cos\delta_i \end{bmatrix} \begin{bmatrix} F^t_{x,i} \\ F^t_{y,i} \end{bmatrix}$$

where δ_i is the steering angle of tire i. The total force acting on the vehicle's centre of mass is obtained by summing all of the tire forces expressed in the vehicle fixed coordinate system. Since the acceleration is expressed in the vehicle fixed coordinate system, the translational acceleration also contains a coupled velocity term caused by the coordinate system rotating with the yaw rate. The longitudinal and lateral accelerations in the vehicle-fixed coordinate system are therefore given by

$$\dot{v}^v_{x,cm} = \frac{\sum F^v_{x,i}}{M} + v^v_{y,CM}\dot{\psi}$$

and

$$\dot{v}^v_{y,cm} = \frac{\sum F^v_{y,i}}{M} - v^v_{x,CM}\dot{\psi}.$$

The yaw acceleration is calculated from the total yaw moment around the centre of mass. Each tire force contributes to the yaw moment depending on the relative position to the centre of mass. The yaw dynamics can then be written as

$$\ddot{\psi} = \frac{M_z}{I_v}$$

where

$$M_z = \sum_i F^v_{y,i}L_{x,i} - F^v_{x,i}L_{y,i} \tag{3.10}$$

Here, $L_{x,i}$ and $L_{y,i}$ are the longitudinal and lateral distances to each tire from the centre of mass as shown in Figure 3.1.

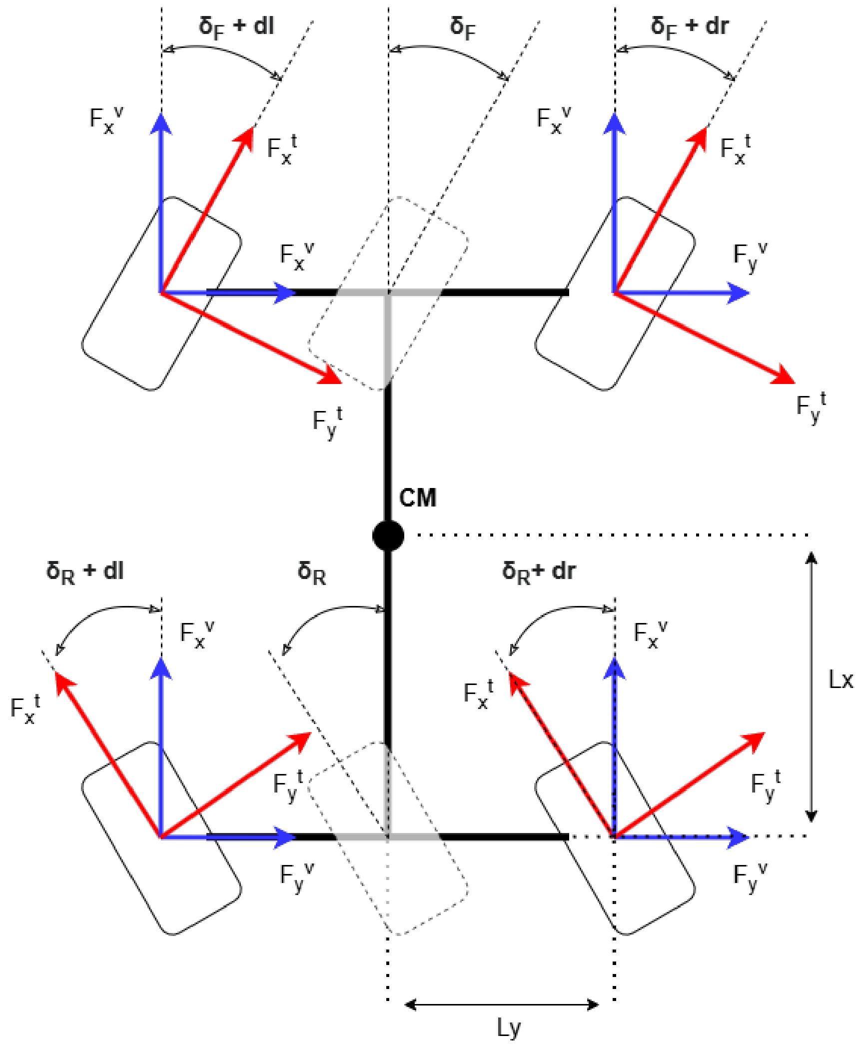

Figure 3.1: Tire steering model forces

The angular acceleration of the wheels is calculated from the torque balance around the rotational axis of the wheels as

$$\dot{w}_i = \frac{T_i - F_{x,rot,i} r}{I_t}$$

Here, $F_{x,rot}$ is is the rotational force caused by τ_x, which is calculated similarly to $F^t_{x,i}$ and $F^t_{y,i}$ in Equations 3.8 and 3.9 using Simpson's 1/3 rule with θ_f, θ_{mid} and θ_r as

$$F_{x,rot,i} = rb\frac{d\theta}{6}\left(\tau_x(\theta_f) + 4\tau_x(\theta_{mid}) + \tau_x(\theta_r)\right)$$

The velocity at each wheel, $v^v_{x,i}$ and $v^v_{y,i}$, is calculated from the velocity at the centre of mass along with the contribution from the yaw rate,

$$v^v_{x,i} = v^v_{x,CM} - \dot{\psi} L_{y,i}$$

$$v^v_{y,i} = v^v_{y,CM} + \dot{\psi} L_{x,i}$$

The wheel velocities are then transformed to the tire fixed coordinate system as

$$\begin{bmatrix} v^t_{x,i} \\ v^t_{y,i} \end{bmatrix} = \begin{bmatrix} \cos\delta_i & \sin\delta_i \\ -\sin\delta_i & \cos\delta_i \end{bmatrix} \begin{bmatrix} v^v_{x,i} \\ v^v_{y,i} \end{bmatrix}$$

which are used to determine λ and β, which are then used to calculate the shear displacements in 3.1.

The steering angles were determined using Ackerman geometry [12] based on the physical vehicle configuration shown in Figure 3.1. Since both the front and rear axles are steered, the instantaneous centre of rotation was defined relative to the midpoint between the two axles, rather than from either the front or rear axle. This gives a symmetric steering geometry that is consistent with the four wheel steering configuration. To represent the actuator dynamics of the physical implementation, where the turning motion is generated by a linear actuator, the steering motion was constrained by a fixed rate limit.

3.1.3 Pivot Steering Vehicle Modelling

The modelling for pivot steering follow the same overall structure as described for tire steering in 3.1.2 except the distances from the centre of mass to the wheels vary with the steering angle. Equation 3.10 is therefore changed to

$$M_z = \sum_{i_a=1}^{2} F^v_{y,A,i_a} l_{x,i_a} \tag{3.11}$$

where F^v_{y,A,i_a} is the lateral force at the axle mid point, defined as

$$F^v_{y,A,1} = \sin\delta_F(F^t_{x,1} + F^t_{x,2}) + \cos\delta_F(F^t_{y,1} + F^t_{y,2})$$

and

$$F^v_{y,A,2} = \sin\delta_R(F^t_{x,3} + F^t_{x,4}) + \cos\delta_R(F^t_{y,3} + F^t_{y,4})$$

for the front and rear axle. The velocity in vehicle frame at each wheel with a static axle, disregarding the rotational speed of each axle, is determined as

$$v^v_{x,i,static} = v^v_{x,cm} - \dot{\psi} L_{y,i}$$

$$v^v_{y,i,static} = v^v_{y,cm} + \dot{\psi} L_{x,i}$$

where $L_{x,i}$ and $L_{y,i}$ are now varying with δ as

$$L_{x,i}(\delta) = l_{x,i_a} - \sin\delta l_{y,i}$$

and

$$L_{y,i}(\delta) = \cos\delta l_{y,i}$$

The velocity in the tire fixed coordinate frame is then determined as

$$\begin{bmatrix} v^t_{x,i} \\ v^t_{y,i} \end{bmatrix} = \begin{bmatrix} \cos\delta_i & \sin\delta_i \\ -\sin\delta_i & \cos\delta_i \end{bmatrix} \begin{bmatrix} v^v_{x,i,static} \\ v^v_{y,i,static} \end{bmatrix} - \begin{bmatrix} \dot{\delta}_F l_{y,i} \\ 0 \end{bmatrix}$$

for the front tires, $i \in \{1, 2\}$, and

$$\begin{bmatrix} v^t_{x,i} \\ v^t_{y,i} \end{bmatrix} = \begin{bmatrix} \cos\delta_i & \sin\delta_i \\ -\sin\delta_i & \cos\delta_i \end{bmatrix} \begin{bmatrix} v^v_{x,i,static} \\ v^v_{y,i,static} \end{bmatrix} - \begin{bmatrix} \dot{\delta}_R l_{y,i} \\ 0 \end{bmatrix}$$

for the rear tires, $i \in \{3, 4\}$, where $\dot{\delta}_F$ and $\dot{\delta}_R$ is the yaw rate for the front and rear axles. These are then used to calculate the shear displacements in 3.1. The angular acceleration for each axle is computed similarly to the yaw acceleration as

$$\ddot{\delta}_F = \frac{\sum_{i=1}^{2}(-F^t_{x,i} l_{y,i})}{I_a}$$

and

$$\ddot{\delta}_R = \frac{\sum_{i=3}^{4}(-F^t_{x,i} l_{y,i})}{I_a}$$

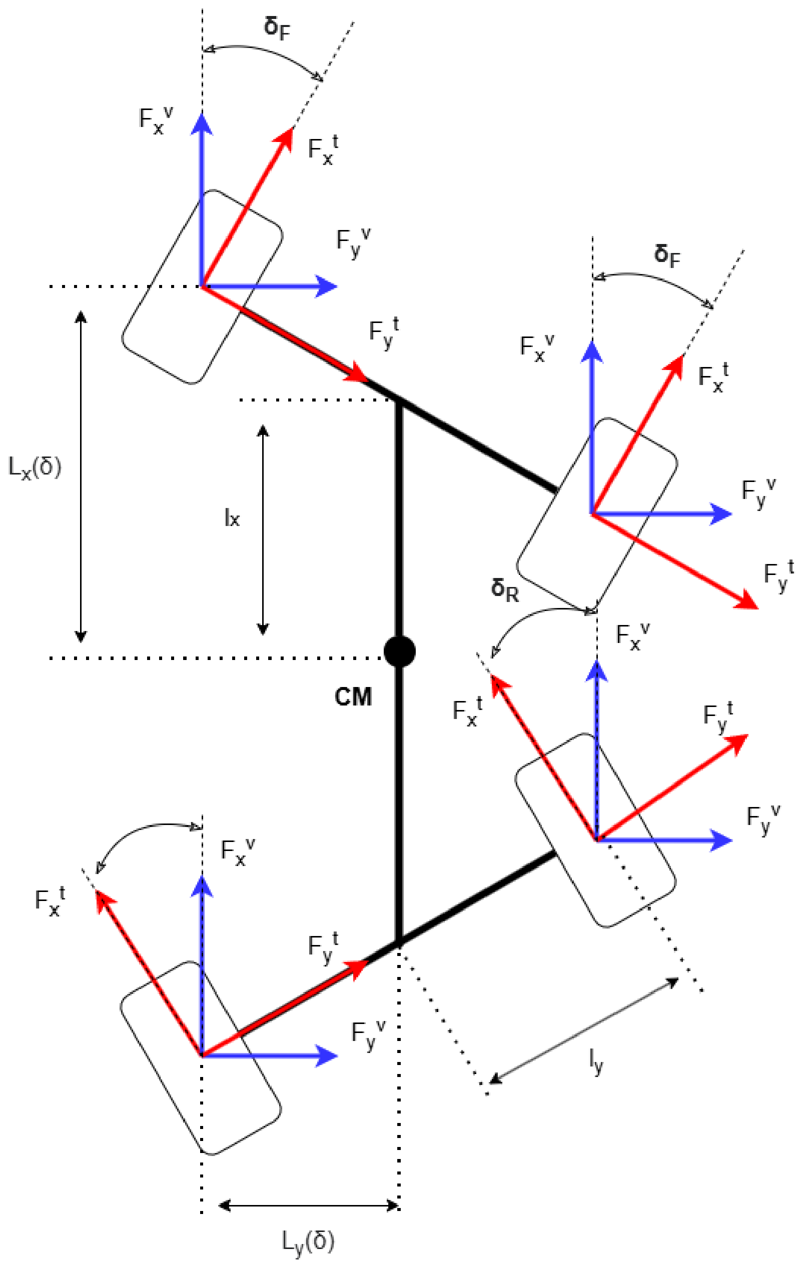

Figure 3.2: Pivot steering model forces

3.2 State Space Formulation

For the controller, the tire forces in Equations 3.8 and 3.9 are approximated using a linear relationship where the longitudinal force is is proportional to the slip rate and the lateral force is proportional to the slip angle,

$$F_{x,i}^t \approx C_x \lambda_i, \quad i = 1:4 \tag{3.12}$$

$$F_{y,i}^t \approx C_y \beta_i, \quad i = 1:4 \tag{3.13}$$

This assumption is mainly relevant when the slip is small. The constants C_x and C_y are approximated as

$$C_x = \left. \frac{\partial F_x}{\partial \lambda} \right|_{\lambda=0}$$

and

$$C_y = \left. \frac{\partial F_y}{\partial \beta} \right|_{\beta=0}$$

3.2.1 Tire Steering State Equations

As the steering is directly controller by the actuators, the steering states are modelled as a first order delay. The delay constant T_c is based on the modelled steering rate limit mentioned in 3.1.2. These are represented using only the steering rate for each axle, δ_F and δ_R. The Ackerman geometry is not modelled and the same steering angle is therefore applied both on the left and right wheel calculations. The state vector then consists of the following

$$x = \begin{bmatrix} v^v_{x,cm} \\ v^v_{y,cm} \\ \dot{\psi} \\ \omega_1 \\ \omega_2 \\ \omega_3 \\ \omega_4 \\ \delta_F \\ \delta_R \end{bmatrix} \tag{3.14}$$

with the non-linear equations as derived in Section 3.1.2

$$\begin{cases} \dot{v}^v_{x,cm} = \frac{1}{M}\left(\sum_{i=1}^4 F^v_{x,i}\right) + v^v_{y,cm}\dot{\psi} \\ \dot{v}^v_{y,cm} = \frac{1}{M}\left(\sum_{i=1}^4 F^v_{y,i}\right) - v^v_{x,cm}\dot{\psi} \\ \ddot{\psi} = \frac{\sum_{i=1}^4 (F^v_{y,i} \cdot L_{x,i} - F^v_{x,i} \cdot L_{y,i})}{I_v} \\ \dot{\omega}_1 = \frac{T_1 - rF^t_{x,1}}{I_t} \\ \dot{\omega}_2 = \frac{T_2 - rF^t_{x,2}}{I_t} \\ \dot{\omega}_3 = \frac{T_3 - rF^t_{x,3}}{I_t} \\ \dot{\omega}_4 = \frac{T_4 - rF^t_{x,4}}{I_t} \\ \dot{\delta}_F = \frac{1}{T_c}(\delta_{F,cmd} - \delta_F) \\ \dot{\delta}_R = \frac{1}{T_c}(\delta_{R,cmd} - \delta_R) \end{cases} \tag{3.15}$$

where $\delta_{F,cmd}$ and $\delta_{R,cmd}$ are the commanded angle inputs.

For the MPC controller, integral states are also included, giving

$$x_{mpc} = \begin{bmatrix} x \\ x_I \end{bmatrix} \tag{3.16}$$

where

$$x_I = \begin{bmatrix} v_{x,e,int} \\ \delta_{F,e,int} \\ \delta_{R,e,int} \end{bmatrix} \tag{3.17}$$

with

$$\begin{cases} v_{x,e,int}(t) = \int_0^t \left(v^v_{x,cm,ref}(\tau) - v^v_{x,cm}(\tau) \right) d\tau \\ \delta_{F,e,int}(t) = \int_0^t \left(\delta_{F,ref}(\tau) - \delta_F(\tau) \right) d\tau \\ \delta_{R,e,int}(t) = \int_0^t \left(\delta_{R,ref}(\tau) - \delta_R(\tau) \right) d\tau \end{cases} \tag{3.18}$$

The inputs to the system is the torque on all wheels along with the commanded steering angle on the front and rear wheels.

$$u = \begin{bmatrix} T_1 \\ T_2 \\ T_3 \\ T_4 \\ \delta_{F,cmd} \\ \delta_{R,cmd} \end{bmatrix} \tag{3.19}$$

As the controller receives a reference velocity $v^v_{x,cm}$ along with references for the front and rear steering angles, δ_F and δ_R, these are chosen as the model outputs, along with the slip ratio λ and slip angle β for each tire. The MPC controller includes the integral states as outputs. For the two controllers, the output vectors are

$$y_{LQR} = \begin{bmatrix} v^v_{x,cm} \\ \lambda_1 \\ \lambda_2 \\ \lambda_3 \\ \lambda_4 \\ \beta_1 \\ \beta_2 \\ \beta_3 \\ \beta_4 \\ \delta_F \\ \delta_R \end{bmatrix} \quad y_{MPC} = \begin{bmatrix} v^v_{x,cm} \\ \lambda_1 \\ \lambda_2 \\ \lambda_3 \\ \lambda_4 \\ \beta_1 \\ \beta_2 \\ \beta_3 \\ \beta_4 \\ \delta_F \\ \delta_R \\ v_{x,e,int} \\ \delta_{F,e,int} \\ \delta_{R,e,int} \end{bmatrix} \tag{3.20}$$

The nonlinear differential equations are then linearized around the steady state operating point, x_0 and u_0, equivalent to the vehicle travelling 1 m/s forward without turning according to Equations 2.22, 2.23.

$$x_0 = \begin{bmatrix} 1 \\ 0 \\ 0 \\ 10 \\ 10 \\ 10 \\ 10 \\ 0 \\ 0 \end{bmatrix} \quad \text{and} \quad u_0 = \begin{bmatrix} 0 \\ 0 \\ 0 \\ 0 \\ 0 \\ 0 \end{bmatrix}$$

It is also discretized with a sampling rate of 10 ms in order to be used in the discrete controllers according to Equations 2.19, 2.20.

3.2.2 Pivot Steering State Equations

For the pivot steering model, two additional integrator states are introduced to model the necessary angle states, as these no longer are directly controlled by an actuator. The resulting state vector then becomes the following

$$x = \begin{bmatrix} v^v_{x,cm} \\ v^v_{y,cm} \\ \dot{\psi} \\ \omega_1 \\ \omega_2 \\ \omega_3 \\ \omega_4 \\ \dot{\delta}_F \\ \dot{\delta}_R \\ \delta_F \\ \delta_R \end{bmatrix} \tag{3.21}$$

with the non linear state equations

$$\begin{cases} \dot{v}^v_{x,cm} = \frac{1}{M}\left(\sum_{i=1}^4 F^v_{x,i}\right) + v^v_{y,cm}\dot{\psi} \\ \dot{v}^v_{y,cm} = \frac{1}{M}\left(\sum_{i=1}^4 F^v_{x,i}\right) - v^v_{x,cm}\dot{\psi} \\ \ddot{\psi} = \frac{\sum_{i_a=1}^2 (F^v_{y,A,i_a} l_{x,i})}{I_v} \\ \dot{\omega}_1 = \frac{T_1 - rF^t_{x,1}}{I_t} \\ \dot{\omega}_2 = \frac{T_2 - rF^t_{x,2}}{I_t} \\ \dot{\omega}_3 = \frac{T_3 - rF^t_{x,3}}{I_t} \\ \dot{\omega}_4 = \frac{T_4 - rF^t_{x,4}}{I_t} \\ \ddot{\delta}_F = \frac{\sum_{i=1}^2 (-F^t_{x,i} l_{y,i})}{I_a} \\ \ddot{\delta}_R = \frac{\sum_{i=3}^4 (-F^t_{x,i} l_{y,i})}{I_a} \\ \dot{\delta}_F = \dot{\delta}_F \\ \dot{\delta}_R = \dot{\delta}_R \end{cases} \tag{3.22}$$

For the MPC controller, the states are again extended with the integral states in Equation 3.17. The steering is no longer directly controlled with the input, so the input vector only consists of the applied torque on each wheel as

$$u = \begin{bmatrix} T_1 \\ T_2 \\ T_3 \\ T_4 \end{bmatrix} \tag{3.23}$$

The outputs y are the same as defined for tire steering in Equation 3.20. The equations are again linearized around the same operating point as for tire steering, using Equations 2.19 and 2.20. The operating points are

$$x_0 = \begin{bmatrix} 1 \\ 0 \\ 0 \\ 10 \\ 10 \\ 10 \\ 10 \\ 0 \\ 0 \\ 0 \\ 0 \end{bmatrix} \quad \text{and} \quad u_0 = \begin{bmatrix} 0 \\ 0 \\ 0 \\ 0 \end{bmatrix}$$

where x_0 and u_0 has been adjusted for the changes in x and u.

3.3 Simulation Environment

The simulation environment was constructed using Simscape and Simulink in Matlab. The environment is divided into three main components: a plant model which handles the vehicle simulation, a filter block with the EKF for estimating the states and a controller block that takes references from a scenario handler block. The overview of the simulation environment is shown in Figure 3.3. The vehicle simulation was modelled using Simscape and consists of a tire block handling the tire and ground interactions as well as a body block which handles the general vehicle movement. The pivot model also contains two additional blocks for the axle simulation. These simulation configurations can be seen in Figure 3.4.

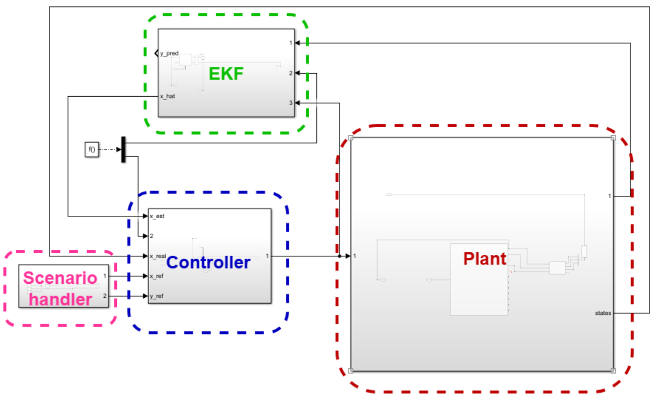

Figure 3.3: Overview of the simulation setup with the controller and filter.

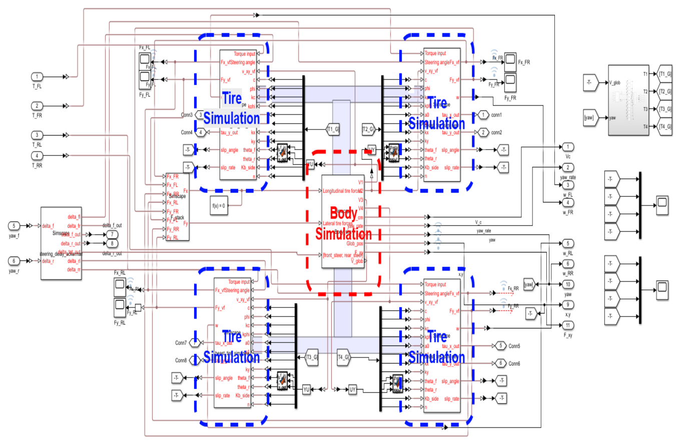

(a) Tire steering model.

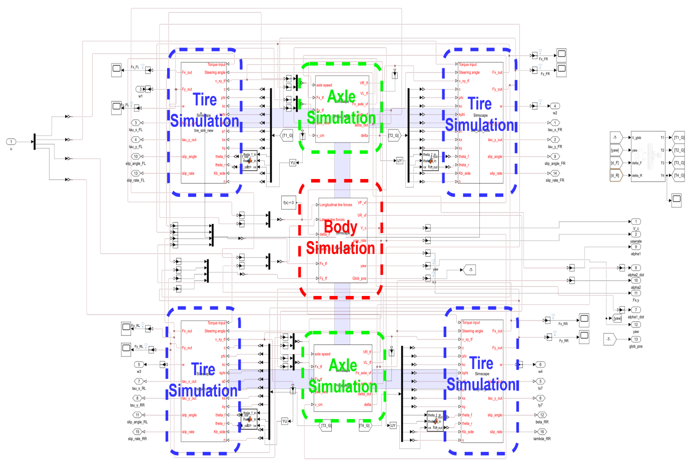

(b) Pivot steering model.

Figure 3.4: Simulation setup in Matlab for the tire and pivot steering models.

3.4 Controller Implementation

3.4.1 LQR

The first controller developed is a discrete time LQR controller, extended with reference feedforward, and with an input increment formulation. The controller is based on the discrete time state space model

$$x(k+1) = A_d x(k) + B_d u(k)$$

where $x(k)$ is the state vector and $u(k)$ is the control input, where k is the discrete time sampled. The control law is then structured as follows

$$u(k) = -Kx(k)$$

Where K is the feedback gain. This formulation regulates the states to the origin. However, Since the objective is to track a non-zero reference, the controller is formulated as a deviation from the steady state operating point. The control law can then be written as

$$u = u_{ss} - K(x - x_{ss})$$

where the feedforward terms x_{ss} is the desired steady state corresponding to the given reference and u_{ss} is the steady state control input required to maintain the reference operating point. The steady-state values were computed using the feedforward matrices K_{xr} and K_{ur}, such that

$$x_{ss}(k) = K_{xr} y_{ref}(k), \qquad u_{ss}(k) = K_{ur} y_{ref}(k).$$

The derivation of these feedforward matrices is given in Appendix A.1. This feed forward input term will be zero for most of the states as the linearized state space does not include any constant friction terms, and no input would therefore be required to keep the reference steady state. However, in the tire steering model a simple first order delay is used to model the steering mechanism and a constant signal is therefore required to achieve a non zero steady state for those states.

With a standard LQR controller with feed forward, the controller could instantly demand a high input when the tracking error changes rapidly. The rapid increase in torque and steering angles could then amount to excessive shear stress when the reference changes abruptly. One possible solution to the problem is to shape the reference signal externally. However, this shifts part of the control problem to the separate external planner. Instead, the controller is formulated using input increments allowing rapid changes in the input to be penalized directly in the LQR cost function. The input increment is defines as

$$\Delta u(k) = u(k) - u(k-1)$$

instead of the absolute value of u. The control action is then updated according to

$$u(k) = u(k-1) + \Delta u(k)$$

The augmented state vector then becomes

$$z_k = \begin{bmatrix} x_k \\ u_{k-1} \end{bmatrix}$$

For tracking around a non zero state, the deviation state is written as

$$\tilde{z}_k = \begin{bmatrix} x_k - x_{\text{ss}} \\ u_{k-1} - u_{\text{ss}} \end{bmatrix}$$

The previous input is treated as an additional state and the augmented state space for the input increment controller then becomes

$$\begin{bmatrix} x(k+1) \\ u(k) \end{bmatrix} = \begin{bmatrix} A_d & B_d \\ 0 & I \end{bmatrix} \begin{bmatrix} x(k) \\ u(k-1) \end{bmatrix} + \begin{bmatrix} B_d \\ I \end{bmatrix} \Delta u$$

The LQR cost function then need to penalise both the state deviation and the deviations from the steady state input. The outputs used in the LQR cost are obtained from the state vector as

$$y_k = Cx(k).$$

For reference tracking, the output deviation is written as

$$\tilde{y}(k) = y(k) - y_{\text{ref}} = C(x(k) - x_{\text{ss}}).$$

The augmented output deviation is then defined as follows

$$\tilde{y}_z(k) = \begin{bmatrix} \tilde{y}(k) \\ u(k-1) - u_{\text{ss}} \end{bmatrix} = \begin{bmatrix} C(x(k) - x_{\text{ss}}) \\ u(k-1) - u_{\text{ss}} \end{bmatrix}.$$

To penalize both the output deviation and the input deviation, the augmented weight matrix is introduced as

$$Q_z = \begin{bmatrix} Q_y & 0 \\ 0 & Q_u \end{bmatrix}.$$

Using this formulation, the cost function becomes

$$J = \sum_{k=0}^{\infty} \left(\tilde{y}_z(k)^\top Q_z \tilde{y}_z(k) + \Delta u(k)^\top R_{\Delta u} \Delta u(k) \right).$$

By inserting the augmented output deviation, the expanded cost function can be written as

$$J = \sum_{k=0}^{\infty} \left((C(x(k) - x_{\text{ss}}))^\top Q_y \left(C(x(k) - x_{\text{ss}}) \right) + (u(k-1) - u_{\text{ss}})^\top Q_u (u(k-1) - u_{\text{ss}}) + \Delta u(k)^\top R_{\Delta u} \Delta u(k) \right).$$

The gain is then computed with the MATLAB function dlqr, which solves the discrete LQR problem. The input deviation controller action is then defined as

$$\Delta u(k) = -K_x \left(x(k) - K_{xr} y_{ref}(k)\right) - K_u \left(u(k-1) - K_{ur} y_{ref}(k)\right)$$

Finally, the total controller input is obtained by adding the input increment to the previous input,

$$u(k) = u(k-1) + \Delta u(k)$$

As the frictional or resistance forces from the ground are not modelled in the state space the feed forward input will be wrong as it assumes no input is required to hold a non zero forward velocity. To reduce this, the input torque needed in the steady state is estimated. This is done by integrating the error $r - Cx$ and adding this to the steady state input u_{ss} which allows it to be non-zero if there are non-modelled external forces.

The resulting block diagram for the controller is seen in Figure 3.5

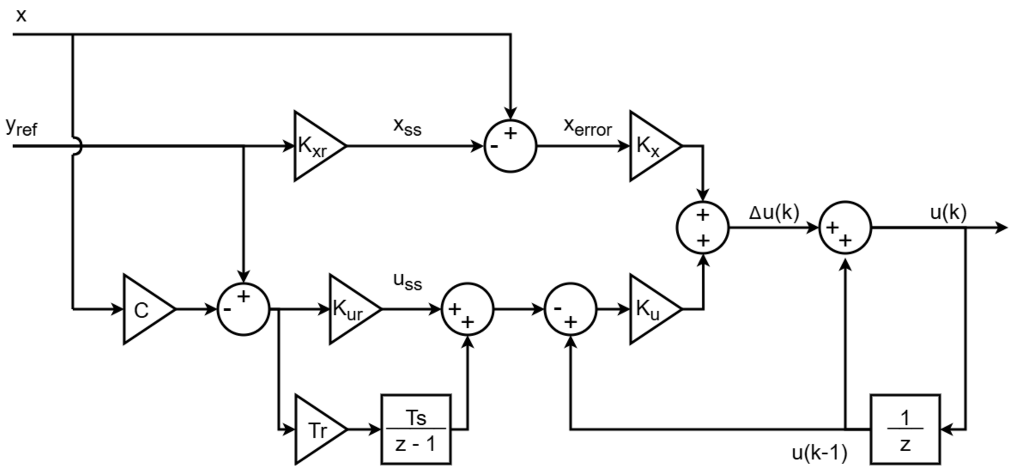

Figure 3.5: LQR controller block diagram

3.4.2 MPC

An MPC controller was developed in order to investigate and compare an alternative model based control method, with the main benefit of being able to handle constraints. The MPC controller was developed using Matlab's `quadprog` function, which solves a quadratic objective function with linear constraints on the form

$$\min_x \frac{1}{2} x^T H x + f^T x \tag{3.24}$$

subject to:

$$A \cdot x \leq b \tag{3.25}$$
$$Aeq \cdot x = beq \tag{3.26}$$
$$lb \leq x \leq ub \tag{3.27}$$

The implemented controller is a linear Model Predictive Controller (MPC) in condensed form. The formulation is based on the discrete-time linear state-space model defined by Equation 2.21. The controller predicts the future system behaviour over a prediction horizon of length N_p. A separate control horizon of length N_c is introduced, where

$$N_c \leq N_p$$

The MPC optimization problem minimizes a finite horizon quadratic cost function based on output tracking errors and control effort as defined in Equation 2.28. For this project, the rate of change of the control inputs and soft constraint violations are added to the cost function, which is modified as

$$J = \sum_{k=1}^{N_p}(y(k)-y_{ref}(k))^T Q_y (y(k)-y_{ref}(k)) + \sum_{k=0}^{N_c-1} u(k)^T R_u u(k) + \sum_{k=0}^{N_c-1} \Delta u(k)^T R_{\Delta u} \Delta u(k) + \rho_\epsilon \epsilon^2$$

where Q_y is the output weighting matrix, R_u is the input weighting matrix, $R_{\Delta u}$ is the input rate weighting matrix, y_{ref} is the output reference signal to be tracked, and ρ_ϵ is a large positive weighting factor penalizing the slack variable ϵ. The additional Δu-term penalizes rapid changes in the control inputs and provides smoother actuator behaviour. In the condensed MPC formulation, the predicted states are not treated as optimization variables. Instead, the future states are expressed explicitly as functions of the initial state and the future control sequence. The predicted outputs can therefore be written in compact form as

$$Y = Fx_0 + \Phi_u U_c$$

where Y is the stacked future output vector, x_0 is the current state, and U_c is the stacked control sequence over the control horizon. The matrices F and Φ_u describe the free response and the forced response of the system. A control horizon N_c is used to reduce the number of optimization variables. For prediction steps beyond the control horizon, the final optimized control input is held constant. The detailed construction of the condensed prediction matrices is provided in Appendix A.2. The finite horizon cost function can be written in compact matrix form as

$$J = (Y - R)^T \bar{Q}_y (Y - R) + U_c^T \bar{R} U_c + (TU_c + d)^T \bar{R}_{\Delta u} (TU_c + d) + \rho_\epsilon \epsilon^2$$

where R is the stacked reference vector, $\bar{Q}_y$ is the lifted output weighting matrix, $\bar{R}$ is the lifted input weighting matrix, and $\bar{R}_{\Delta u}$ is the lifted input rate weighting matrix. The matrix T and vector d are used to express the stacked input increments as a function of the optimized control sequence U_c and the previously applied input $u(-1)$. The full derivation of the compact cost function and its conversion to the quadratic programming form used by `quadprog` is shown in Appendix A.2. Input constraints are incorporated as hard linear inequality constraints. Upper and lower bounds are imposed on the control inputs according to

$$u_{\min} \leq u(k) \leq u_{\max}, \quad k = 0, \ldots, N_c - 1$$

In addition, constraints are imposed on selected predicted outputs. To improve robustness and avoid overly aggressive behaviour near the constraint boundaries, the output constraints are implemented as soft constraints using the slack variable ϵ. The softened output constraints are written as

$$y_{\min} - \epsilon \leq y_c(k) \leq y_{\max} + \epsilon, \quad k = 1, \ldots, N_p$$

with

$$\epsilon \geq 0.$$

Here, $y_c(k)$ denotes the selected constrained outputs at prediction step k. This allows the controller to temporarily violate the output constraints if necessary, while still penalizing the violation through the term $\rho_\epsilon \epsilon^2$ in the cost function. The detailed matrix formulation of the input and output constraints is given in Appendix A.2. After constructing the Hessian, gradient vector, and inequality constraints, the quadratic program is solved using Matlab's `quadprog` solver with the active-set algorithm. The previous optimal solution is used as an initial guess for the optimization, which provides warm-starting and improves computational efficiency. After each optimization step, the optimal control sequence is shifted forward by one control interval and reused as the initial guess for the next optimization problem. The optimizer returns the optimal future control sequence

$$U_c^\star = \begin{bmatrix} u(0)^\star \\ u(1)^\star \\ \vdots \\ u(N_c - 1)^\star \end{bmatrix}$$

The first control input $u(0)^\star$ is applied to the system. At the next sampling instant, the system state is measured again and the optimization problem is solved repeatedly using updated state information.

3.5 Filter Implementation

The filter was constructed using the same non linear state space as for the controller modelling, with minor modifications to avoid numerical problems caused by division by small values at standstill. As the current implemented vehicles does not have an IMU, only the wheel speeds are used as measurements for movement. In the pivot steering model, the front and rear steering angles are also measured, whereas in the tire steering model, the steering angles are assumed to follow the commanded controller inputs and are therefore not included in the measurement vector. The filter is then constructed according the EKF equations in Section 2.2.5.

The measured output vectors for the pivot and tire steering models are defined as

$$y_{Pivot}(k) = \begin{bmatrix} \omega_1(k) \\ \omega_2(k) \\ \omega_3(k) \\ \omega_4(k) \\ \delta_F(k) \\ \delta_R(k) \end{bmatrix} \quad y_{Tire}(k) = \begin{bmatrix} \omega_1(k) \\ \omega_2(k) \\ \omega_3(k) \\ \omega_4(k) \end{bmatrix} \tag{3.28}$$

.

Since the measurements quantifies directly available states, the measurement functions are linear and only select the corresponding entries from the state vector. They are therefore given by

$$h_{\text{Pivot}}(x(k)) = \begin{bmatrix} x_4(k) \\ x_5(k) \\ x_6(k) \\ x_7(k) \\ x_{10}(k) \\ x_{11}(k) \end{bmatrix}, \qquad h_{\text{Tire}}(x(k)) = \begin{bmatrix} x_4(k) \\ x_5(k) \\ x_6(k) \\ x_7(k) \end{bmatrix}. \tag{3.29}$$

3.6 Evaluation Method

The evaluation method aims at evaluating both the impact on the ground of pivot steering compared to tire steering and the performance and robustness of the developed controllers. Table 3.1 shows the values for the ground parameters of the ground types used for testing [3]. The majority of the tests were conducted on sandy loam, which is a type of soil that contains a mix of sand, silt and clay. It is used for farming and gardening and is sensitive to excessive shear stress.

Table 3.1: Ground parameters for sandy loam and heavy clay.

Parameter	Description	Sandy loam	Heavy clay	Unit
c	Cohesion stress	1720	20690	Pa
K	Soil deformation	0.01	0.005	m
ϕ	Friction angle	0.5061	0.1047	rad
k_c	Cohesive modulus	$5.27 \cdot 10^3$	$1.84 \cdot 10^3$	N/m^{n+1}
k_ϕ	Frictional modulus	$1515 \cdot 10^3$	$103.27 \cdot 10^3$	N/m^{n+2}
n	Sinkage exponent	0.7	0.11	
a_0		0.4	0.4	
a_1		0.15	0.15	
ρ	Soil density	18000	18000	kg/m^3
Λ	Wheel sinkage ratio	0.9	0.9	

Both the soil density ρ and the wheel sinkage ratio Λ are set to the same value for both types of soil. This is because there is no information on the exact density or sinkage ratio for the different soils and these are difficult to determine without further testing of the specific materials. The parameters a_0 and a_1 are also set to assumed values and are not changed for the two ground types for the same reason.

This causes some inaccuracies in the simulation, but was determined to be functional as the other parameters varies and the main goal is to gather results for the behaviour under changing conditions rather than achieve an exact representation of real-world operation. The static contact angle θ_s for each tire is determined numerically in Matlab using Equation 2.6. The corresponding static sinkage h_s is calculated with Equation 2.7. Dynamic sinkage is not considered and, therefore, $h = h_s$ when the vehicle is in standstill and when moving. The entry angle θ_f and exit angle θ_r are determined using Equations 2.8 and 2.9. The resulting values are shown in table 3.2.

Table 3.2: Static sinkage and wheel contact angles for sandy loam and heavy clay.

Ground type	h_s (m)	θ_s (rad)	θ_f (rad)	θ_r (rad)
Sandy loam	0.0031	0.2480	0.2480	-0.2352
Heavy clay	0.0005	0.0993	0.0993	-0.0942

3.6.1 Vehicle Parameter Values

The total mass for the vehicle, M, mass at each wheel m, wheel radius r, tire width b, and lengths l_x and l_y were measured from the physical tire steering model. The moment of inertia for both the axle and the body, were calculated using Steiner's theorem [13]. To ensure a consistent comparison between the tire steering and pivot steering models, the same inertia calculation procedure and measured dimensions were used for both models. The distances from the centre of mass were taken from Figure 3.6a, and the cross-sectional dimensions of the model frame are shown in Figure 3.6b. The body frame was constructed out of steel with an assumed density of 8000 kg/m^3, the mass of the wheels and boxes located in the front and rear of the vehicle was set to 1.5 kg and 15 kg for the simulation. The measurements and calculated parameters can be seen in Table 3.3.

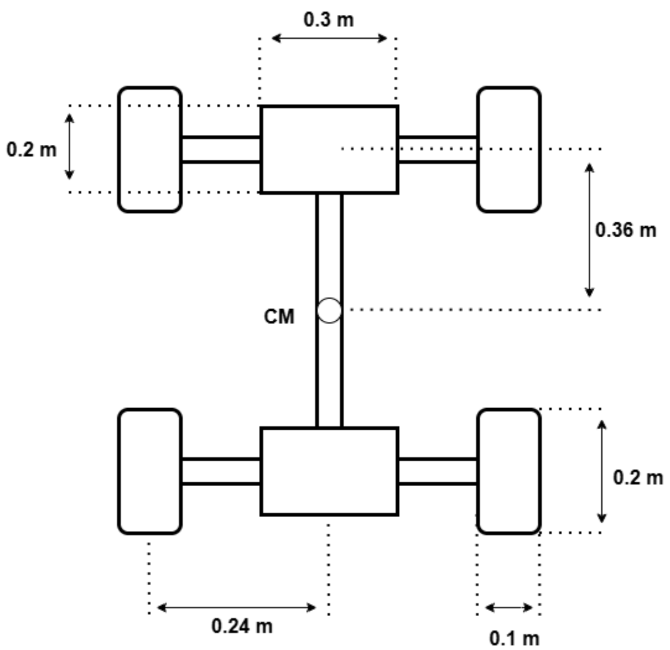

(a) Measurements of model.

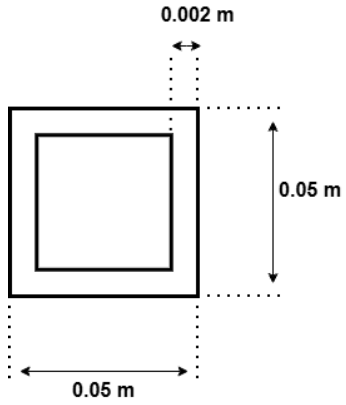

(b) Cross section of model frame.

Table 3.3 shows the values for the different vehicle parameters that are used for testing.

Table 3.3: Table of vehicle parameters.

Parameter	Value	Unit
M	40	kg
m	10	kg
r	0.1	m
b	0.1	m
I_v	12.8	kg· m^2
I_a	2.2	kg· m^2
I_t	0.007	kg· m^2
l_x	0.35	m
l_y	0.24	m

3.6.2 Evaluation Metrics

Below are the definitions for the evaluation metrics used in Section 3.6.3. The tests performed evaluated one or multiple of these metrics.

3.6.2.1 Ground Impact Metrics

The sum of the longitudinal and lateral shear stress for a tire at a discrete time step k is calculated as

$$\tau_{x,tot}(k) = \sum_{i=1}^{4} |\tau_{x,i}(k)| \tag{3.30}$$

and

$$\tau_{y,tot}(k) = \sum_{i=1}^{4} |\tau_{y,i}(k)| \tag{3.31}$$

where $\tau_{x,i}$ and $\tau_{y,i}$ is the longitudinal and lateral shear stress for each tire. The resulting shear stress for a tire is calculated as

$$\tau_i(k) = \sqrt{\tau_{x,i}^2(k) + \tau_{y,i}^2(k)} \tag{3.32}$$

The RMS value for the total resulting shear stress for the vehicle after N samples can be determined as

$$\tau_{RMS} = \sqrt{\frac{1}{N}\sum_{k=1}^{N} \tau_{tot}^2(k)}, \tag{3.33}$$

where $\tau_{tot}(k)$ is defined as

$$\tau_{tot}(k) = \sum_{i=1}^{4} \tau_i(k) \tag{3.34}$$

The peak shear stress value reached by any tire for a given interval $\mathcal{I}_p$ is defined as

$$\tau_{\text{peak}}^{(p)} = \max_{\substack{i=1,\ldots,4 \\ k\in\mathcal{I}_p}} |\tau_i(k)| \tag{3.35}$$

3.6.2.2 Performance Metrics

To evaluate the reference tracking performance of the controllers, the RMSE values for the longitudinal velocity $v_{x,cm}^v$, and steering angles δ_f and δ_R are defined for a test case as follows,

$$v_{RMSE} = \sqrt{\frac{1}{N}\sum_{k=1}^{N}(v_{x,cm,ref}^v(k) - v_{x,cm}^v(k))^2} \tag{3.36}$$

$$\delta_{FRMSE} = \sqrt{\frac{1}{N}\sum_{k=1}^{N}(\delta_{F,ref}(k) - \delta_F(k))^2} \tag{3.37}$$

$$\delta_{RRMSE} = \sqrt{\frac{1}{N}\sum_{k=1}^{N}(\delta_{R,ref}(k) - \delta_R(k))^2} \tag{3.38}$$

where N denotes the number of samples in the evaluated time interval. The rise time from 10 % to 90 % of the reference value for $v_{x,cm}^v$ and δ_F are determined as

$$t_{r,v} = t_{v_{x,cm}^v,90\%} - t_{v_{x,cm}^v,10\%} \tag{3.39}$$

and

$$t_{r,\delta} = t_{\delta_F,90\%} - t_{\delta_F,10\%} \tag{3.40}$$

A maximum error for $v_{x,cm}^v$ for a certain evalation interval $\mathcal{I}_p$ is calculated as

$$e_{v,\max}^{(p)} = \max_{k\in\mathcal{I}_p} \left| v_{x,cm,\text{ref}}^v(k) - v_{x,cm}^v(k) \right| \tag{3.41}$$

The peak values for λ and β reached for any tire are defined as

$$\lambda_{peak} = \max_{i,k} |\lambda_i(k)| \tag{3.42}$$

and

$$\beta_{peak} = \max_{i,k} |\beta_i(k)| \tag{3.43}$$

where $i \in \{1, \ldots, 4\}$ and $k \in \{1, \ldots, N\}$.
The RMSE values for the estimated and simulated state vales are defined as

$$x_{\mathrm{RMSE}_i} = \sqrt{\frac{1}{N}\sum_{k=1}^{N}\left(x(k) - \hat{x}(k)\right)^2} \tag{3.44}$$

where $i \in \{v_x, v_y, \dot{\psi}, \omega_1, \omega_2, \omega_3, \omega_4, \dot{\delta_F}, \dot{\delta_R}, \delta_F, \delta_R\}$

3.6.3 Test Cases

The following is a description of the different test cases that were conducted and the evaluation metrics recorded for each test. All tests were conducted in the simulation environment described in Section 3.3.

3.6.3.1 Steering Configurations Test

To compare the impact on the ground of the two different steering configurations, a constant-velocity turn was performed at $v^v_{x,cm} = 1$ m/s, $\delta_F = 0.436$ rad and $\delta_R = -0.436$ rad. The goal of the test was to obtain a comparison of the two steering configurations in the absence of control impact. The sum of the lateral and longitudinal shear stresses, $\tau_{x,tot}$ and $\tau_{y,tot}$, defined by Equations 3.30 and 3.31, were reported together with the resulting yaw rate $\dot{\psi}$ of the vehicle. To obtain a more detailed comparison between the two steering methods, a second constant turn test was conducted where the pivot steering vehicle was tuned to reach an identical yaw rate as the tire steering vehicle. Again, $\tau_{x,tot}$ and $\tau_{y,tot}$ was reported.

3.6.3.2 Controller Verification and Tuning

To evaluate that the developed controllers behave as expected for both tire steering and pivot steering while simultaneously tuning the controllers, a simple reference tracking test was conducted. The PI, LQR and MPC controllers were tuned for each steering configuration, resulting in six tests in total. For the test scenario, the vehicle started from standstill and was given a forward reference velocity of $v^v_{x,cm,ref} = 1$ m/s after 1 second. After 10 seconds, steering angle references of $\delta_{F,ref} = 0.25$ rad and $\delta_{R,ref} = -0.25$ were set for the front and rear tires respectively, while the forward velocity reference was maintained. The simulation was stopped after 15 seconds.

Since ground impact is of main importance, the controllers were tuned based on the value of the total shear stress τ_i for each tire, defined in 3.32. The simulation was divided into two evaluation intervals: the acceleration phase $\mathcal{I}_{acc}$ for $t \in [1, 10]$ s and the turning phase $\mathcal{I}_{turn}$ for $t \in [10, 15]$ s. The controllers were tuned such that the peak shear stress, defined in Equation 3.35, satisfies

$$\tau_{\text{peak}}^{(p)} = 0.25 \cdot \tau_{\max}, \quad p \in \{acc, turn\}. \tag{3.45}$$

The test was conducted on sandy loam, view table 3.1, where $\tau_{\max} = 9428\,\text{N/m}^2$ for each tire. The LQR controller was tuned first where Bryson's rule [14] was used as a starting point for determining the initial weighting matrices Q_y and $R_{\Delta u}$, as

$$Q_{y,ii} = \frac{1}{e_{i,\max}^2}$$

$$R_{\Delta u,jj} = \frac{1}{\Delta u_{j,\max}^2}$$

where $e_{i,\max}$ is the maximum acceptable error for output y_i and $\Delta u_{j,\max}$ is the maximum acceptable control input rate. The weights were then adjusted based on the criterion for $\tau_{\text{peak}}^{(acc)}$ and $\tau_{\text{peak}}^{(turn)}$. The weights for Q_u were used as the main tool for tuning and were not based on Bryson's rule. No weights were set for slip ratio λ and slip angle β as that is investigated in Section 3.6.3.4.

The weights determined for the LQR controller were used as a starting point when tuning the MPC. For the MPC controller, the prediction horizon N_p and control horizon N_c were determined in an iterative process. To determine N_p, the control horizon was kept fixed at $N_c = 2$ while N_p was increased in steps of ten, $N_p = \{10, 20, 30...\}$, until further increases did not have a major impact on performance. Then N_c was iteratively increased as $N_c = \{1, 2, 3...\}$. Finally, the weights for Q_y and R_u were adjusted until the criterion for $\tau_{\text{peak}}^{(acc)}$ and $\tau_{\text{peak}}^{(turn)}$ was also fulfilled for the MPC controller. The weights for $R_{\Delta u}$ were kept from the LQR tuning for simplicity. For the PI controller, the proportional gain constant was tuned based on the criterion for $\tau_{\text{peak}}^{(acc)}$ and $\tau_{\text{peak}}^{(turn)}$. For all three controllers, integral action was applied to remove steady state errors.

The reference tracking performance for the longitudinal velocity $v_{x,cm}^v$ and steering angles δ_F and δ_R was plotted, as well as the shear stress τ for each tire. The rise times $t_{r,v}$ and $t_{r,\delta}$, together with the maximum velocity error $e_{v,\max}^{(\text{turn})}$ for $\mathcal{I}_{turn}$, described by Equations 3.39-3.41, were also reported. Finally, the RMSE values v_{RMSE}, $\delta_{F_{RMSE}}$ and $\delta_{R_{RMSE}}$, described by Equations 3.36-3.38, were also reported, as well as τ_{RMS}, defined by Equation 3.34. These performance metrics do not have required limits but were noted to determine if the criterion for $\tau_{\text{peak}}^{(acc)}$ and $\tau_{\text{peak}}^{(turn)}$ could be deemed reasonable and used as comparative metrics between the different tests. The extended kalman filter was evaluated in a separate test and was not used. Therefore, no uncertainty in the states was assumed. The controller weights acquired from this test were used for the rest of the tests apart from in 3.6.3.4, where the effect of non-zero weights on slip ratio λ and slip angle β was investigated.

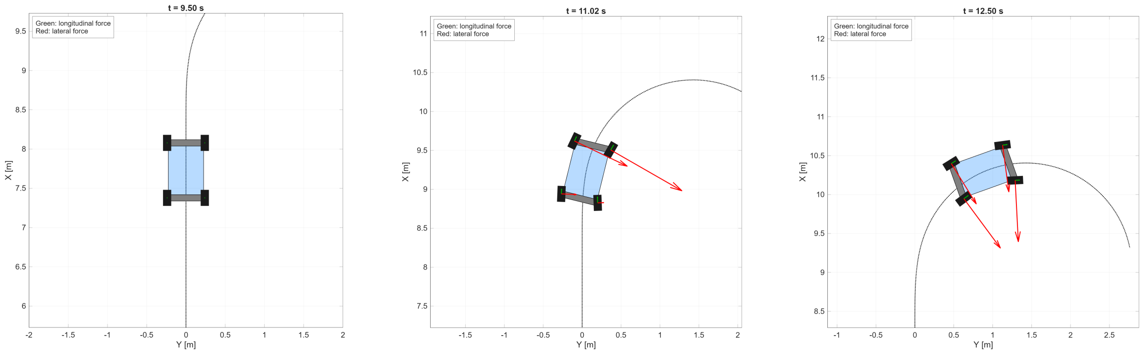

(a) **(b)** **(c)**

Figure 3.7: Illustration of the tuning test for the tire steering model. The vehicle starts of from standstill, begins accelerating to 1 m/s after 1 second, and starts steering to $\delta_F = 0.25$ rad and $\delta_R = -0.25$ rad after 10 seconds

3.6.3.3 Asymmetric Terrain Conditions Test

To evaluate the performance of the tuned LQR and MPC controllers for tire steering and pivot steering in varying conditions, a test was conducted where the right hand tires enter an area with a different ground type. For each steering configuration, the PI, LQR and MPC controllers were evaluated, resulting in six test cases in total. A forward reference velocity was set to $v^v_{x,cm,ref} = 1$ with no steering references. After the vehicle has travelled 5 meters, the right hand side tires enter an area with heavy clay, view table 3.1. The reference tracking performance for $v^v_{x,cm}$, δ_F and δ_R was plotted, as well as the shear stress τ for each tire. The performance metrics v_{RMSE}, $\delta_{F_{RMSE}}$, $\delta_{R_{RMSE}}$ and τ_{RMS} were recorded.

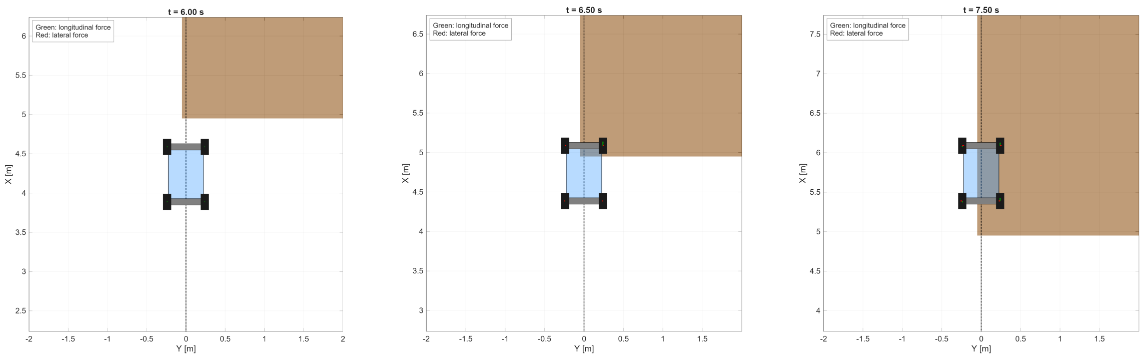

(a) **(b)** **(c)**

Figure 3.8: Illustration of the asymmetric terrain test. The vehicle starts of on uniform ground (white), later the right side drives into a different type of terrain (brown)

3.6.3.4 Slip Weights Test

To investigate the slip reduction capabilities of the model based controllers, a series of tests were conducted using both tire steering and pivot steering configurations. For each steering configuration, the LQR and MPC controllers were evaluated using three different weighting values applied for the slip ratio λ and slip angle β on all tires. The weighting values tested were 500, 2500, and 5000, resulting in six test cases per steering configuration and twelve test cases in total. The test scenario was identical to that described in Section 3.6.3.2. For each controller and steering configuration, the peak values λ_{peak} and β_{peak}, defined by Equations 3.42 and 3.43, were recorded together with $\tau_{peak}^{(acc)}$ and $\tau_{peak}^{(turn)}$. In addition, the performance metrics v_{RMSE}, $\delta_{F_{RMSE}}$, $\delta_{R_{RMSE}}$ and τ_{RMS} were reported.

3.6.3.5 MPC Constraints Test

The MPC controller allows for the use of constraints on both the controlled outputs, y, and inputs, u. As the slip ratio λ and slip angle β are directly related to the lateral and longitudinal shear stress, a test was conducted where these outputs were constrained in the MPC controller for both tire and pivot steering for the same test scenario as described in 3.6.3.2. The constraints were set to $\lambda = 0.08$ and $\beta = 0.08$ rad on each tire. The peak values λ_{peak}, β_{peak}, $\tau_{peak}^{(acc)}$ and $\tau_{peak}^{(turn)}$ were recorded as well as the rise times $t_{r,v}$ and $t_{r,\delta}$, together with the maximum velocity error $e_{v,\max}^{(\text{turn})}$. The values for v_{RMSE}, $\delta_{F_{RMSE}}$, $\delta_{R_{RMSE}}$ and τ_{RMS} were also reported. Finally, the reference tracking performance for $v_{x,cm}^{v}$, δ_F and δ_R was plotted, as well as the shear stress τ for each tire.

3.6.4 EKF Test

The EKF was tested in two parts. First, the estimated states were compared with the simulated states according to 3.44 in order to see how accurate the filter is as estimating both the measured and non measured states. Secondly, the LQR controller was used together with the estimated states and the tracking abilities were evaluated using the RMSE for the longitudinal velocity and the steering angles using Equations 3.36, 3.37 and 3.38. Gaussian noise was applied to the wheel angular velocities with zero mean and variance of 0.1 for both steering configurations. The pivot steering had a noise with zero mean and variance of 0.01 applied to the angle measurements.

4

Results

4.1 Steering Configurations Test

Table 4.1a shows the total shear stresses $\tau_{x,tot}$ and $\tau_{y,tot}$ and vehicle yaw-rate $\dot{\psi}$ for the test described in 3.6.3.1. The values for both $\tau_{x,tot}$ and $\tau_{y,tot}$ are higher for the tire steering model compared to the pivot steering model. The value for $\dot{\psi}$ is also higher for tire steering. Table 4.1b shows the resulting values for $\tau_{x,tot}$ and $\tau_{y,tot}$ for the pivot steering model with steering angles changed to $\delta_F = 0.4415$ and $\delta_R = -0.4415$, resulting in the same value for $\dot{\psi}$ as the tire steering model in table 4.1a. Again, it can be noted that the values for $\tau_{x,tot}$ and $\tau_{y,tot}$ are less than for tire steering.

Table 4.1: Comparison of total longitudinal and lateral shear stress, $\tau_{x,tot}$ and $\tau_{y,tot}$, and yaw rate $\dot{\psi}$ for the tire steering and pivot steering configurations during a constant velocity turn at $v^v_{x,cm} = 1$ m/s.

(a) Total longitudinal and lateral shear stress and vehicle yaw rate for tire steering and pivot steering with $\delta_F = 0.436$ rad and $\delta_R = -0.436$ rad.

Steering configuration	$\tau_{x,tot}$ (N/m^2)	$\tau_{y,tot}$ (N/m^2)	$\dot{\psi}$ (rad/s)
Tire steering	3797	14070	1.5045
Pivot steering	3294	13316	1.4741

(b) Total longitudinal and lateral shear stress for pivot steering when operated at the same yaw rate as the tire steering case in Table 4.1a.

Steering configuration	$\tau_{x,tot}$ (N/m^2)	$\tau_{y,tot}$ (N/m^2)	$\dot{\psi}$ (rad/s)
Pivot steering	3454	13629	1.5045

4.2 Controller Verification and Tuning

4.2.1 LQR Tuning

The controller was tuned based on the method described in 3.6.3.2. The values for Q_y and $R_{\Delta u}$ were based on Bryson's rule, where the maximum acceptable error for $v^v_{x,cm}$ was set to 0.04 m/s and the maximum acceptable error for δ_F and δ_R was set to 0.02 rad, resulting in the initial values $Q_{y,1,1} = 625$ and $Q_{y,10,10} = Q_{y,11,11} = 2500$. The maximum allowed input rate for the torques on each wheel was initially set to 1 Nm/s and the diagonal elements of the weighting matrix $R_{\Delta u}$ corresponding to the torques were therefore set to 10000 given the sampling time of 10 ms. For tire steering, the maximum allowed input rate was set to 0.001 rad/s and the diagonal elements of $R_{\Delta u}$ corresponding to the steering angles were therefore set to 10^6 initially. The weights were adjusted together with Q_u based on the criterion for $\tau_{\text{peak}}^{(acc)}$ and $\tau_{\text{peak}}^{(turn)}$. Table 4.2 shows the final weights determined for the LQR controller for tire and pivot steering.

Table 4.2: Final LQR controller tuning weights for tire and pivot steering.

Tire steering LQR weights

$$\begin{aligned} Q_y &= \text{diag}(625, 0, 0, 0, 0, 0, 0, 0, 0, 2500, 2500), \\ Q_u &= \text{diag}(47, 47, 47, 47, 100, 100), \\ R_{\Delta u} &= \text{diag}(10^4, 10^4, 10^4, 10^4, 4.7 \cdot 10^6, 4.7 \cdot 10^6). \end{aligned}$$

Pivot steering LQR weights

$$\begin{aligned} Q_y &= \text{diag}(625, 0, 0, 0, 0, 0, 0, 0, 0, 3100, 3100), \\ Q_u &= \text{diag}(47, 47, 47, 47), \\ R_{\Delta u} &= \text{diag}(10^4, 10^4, 10^4, 10^4). \end{aligned}$$

Figures 4.1a and 4.1b shows the resulting reference tracking performance for tire and pivot steering respectively. It can be observed that $v_{x,cm}^v$ decreases during initial turning for both steering configurations.

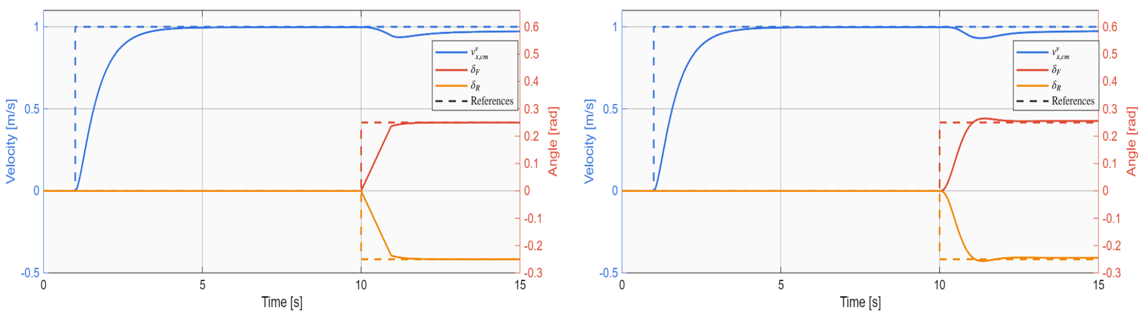

(a) Tire steering configuration.

(b) Pivot steering configuration.

Figure 4.1: Reference tracking of the longitudinal velocity v_{cm}^x and the steering angles δ_F and δ_R for the tire steering and pivot steering configurations using the tuned LQR controller.

Figure 4.2 shows the resulting shear stress τ for each tire for the tire steering and pivot steering model. It can be observed that the requirements for $\tau_{\text{peak}}^{(acc)}$ and $\tau_{\text{peak}}^{(turn)}$ are fulfilled. For the turning phase, the front right tire reaches the highest value for τ.

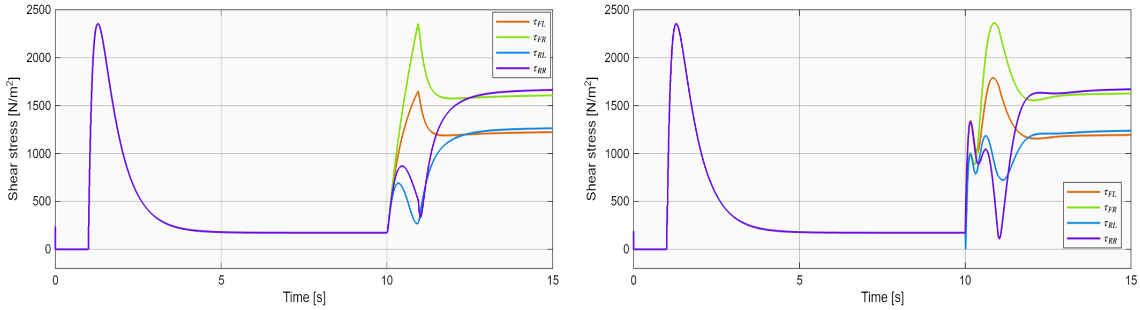

(a) Tire steering configuration.

(b) Pivot steering configuration.

Figure 4.2: Shear stress τ for each tire during the LQR tuning test for the tire steering and pivot steering configurations.

Table 4.5a shows the rise times $t_{r,v}$ and $t_{r,\delta}$ as well as the maximum velocity tracking error during the turning phase, $e_{v,max}^{(turn)}$, for pivot steering and tire steering using the tuned LQR controller. It can be noted that $t_{r,v}$ is close to identical for the two steering configurations. On the other hand, $t_{r,\delta}$ differs more clearly with a higher value for tire steering which in turn leads to a slightly reduced value of $e_{v,max}^{(turn)}$. Table 4.5b shows the values for v_{RMSE}, δ_{FRMSE}, δ_{RRMSE} and τ_{RMS}.

Table 4.3: Performance metrics for tire steering and pivot steering using the LQR controller.

(a) Rise times for $v_{x,cm}^{v}$ and δ_F, and maximum velocity tracking error during turning for the different steering configurations.

Steering configuration	$t_{r,v}$ (s)	$t_{r,\delta}$ (s)	$e_{v,max}^{(turn)}$ (m/s)
Tire steering	1.4141	0.8000	0.0633
Pivot steering	1.4139	0.6402	0.0696

(b) RMSE value for $v_{x,cm}^{v}$, δ_F and δ_R, and RMS value for τ_{tot} for the two steering configurations.

Steering configuration	v_{RMSE} (m/s)	δ_{FRMSE} (rad)	δ_{RRMSE} (rad)	τ_{RMS} (N/m^2)
Tire steering	0.1725	0.0376	0.0376	3014
Pivot steering	0.1726	0.0416	0.0417	2766

4.2.2 MPC Tuning

The MPC controller was tuned based on the method described in 3.6.3.2. The control horizon was initially determined to $N_p = 50$ and the control horizon to $N_c = 5$, which resulted in similar behaviour as the LQR controller. A lower N_p resulted in overshooting and no major impact on performance was noted when increasing N_p beyond 50. For pivot steering, the peak shear stress requirement for the turning phase, $\tau_{\text{peak}}^{(turn)} = 0.25 \cdot \tau_{max}$, was not achievable with this prediction horizon and it was therefore increased to $N_p = 70$. For tire steering it was kept at $N_p = 50$. The resulting MPC weights are shown in table 4.4.

Table 4.4: Final MPC controller tuning weights for tire and pivot steering.

Tire steering MPC weights

$$
\begin{aligned}
Q_y &= \text{diag}(625, 0, 0, 0, 0, 0, 0, 0, 0, 2500, 2500, 500, 0, 0), \\
R_u &= \text{diag}(118, 118, 118, 118, 100, 100), \\
R_{\Delta u} &= \text{diag}(10^4, 10^4, 10^4, 10^4, 2 \cdot 10^6, 2 \cdot 10^6).
\end{aligned}
$$

Pivot steering MPC weights

$$
\begin{aligned}
Q_y &= \text{diag}(625, 0, 0, 0, 0, 0, 0, 0, 0, 1.45 \cdot 10^4, 1.45 \cdot 10^4, 500, 0, 0), \\
R_u &= \text{diag}(142, 142, 142, 142), \\
R_{\Delta u} &= \text{diag}(10^4, 10^4, 10^4, 10^4).
\end{aligned}
$$

Figure 4.3 shows the resulting reference tracking performance for tire steering and pivot steering respectively. Again, $v^v_{x,cm}$ decreases during the initial turning for both steering configurations.

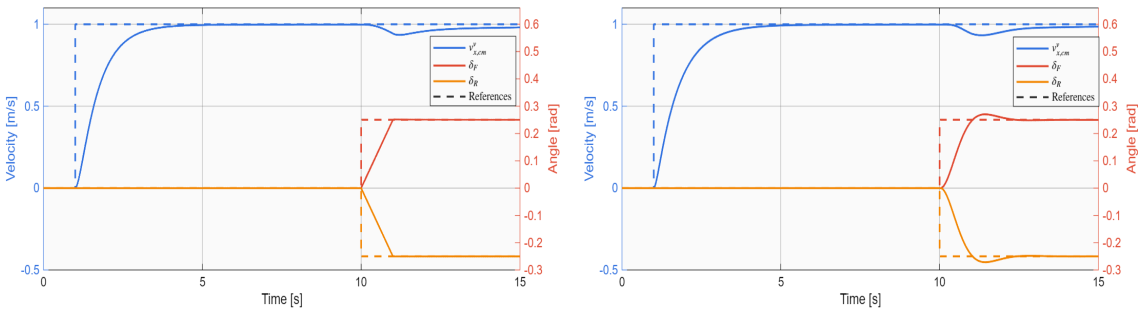

(a) Tire steering configuration. **(b)** Pivot steering configuration.

Figure 4.3: Reference tracking of the longitudinal velocity v^x_{cm} and the steering angles δ_F and δ_R for the tire steering and pivot steering configurations using the tuned MPC.

Figure 4.4 below shows the resulting shear stress τ for each tire for tire steering and pivot steering with the tuned MPC controller.

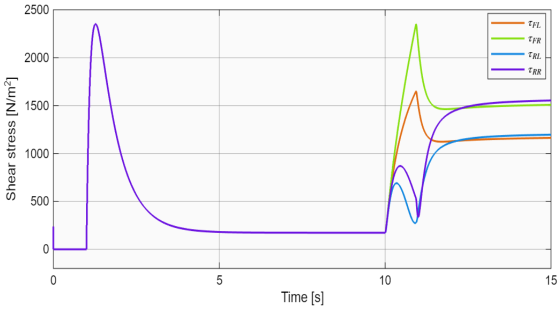

(a) Tire steering configuration.

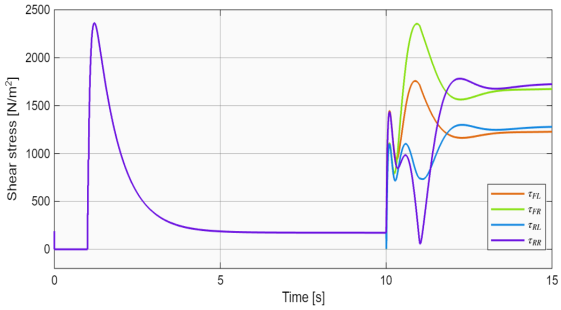

(b) Pivot steering configuration.

Figure 4.4: Shear stress τ for each tire during the MPC tuning test for the tire steering and pivot steering configurations.

Table 4.5a shows the rise times $t_{r,v}$ and $t_{r,\delta}$ as well as the maximum velocity tracking error during the turning phase, $e_{v,max}^{(turn)}$, for pivot steering and tire steering using the MPC controller. It can be noted that $t_{r,v}$ differs significantly between the two steering configurations, which is a result of the higher prediction horizon and weights in R_y required for the pivot steering to achieve the requirement for $\tau_{\text{peak}}^{(turn)}$. Table 4.5b shows the values for v_{RMSE}, δ_{FRMSE}, δ_{RRMSE} and τ_{RMS}.

Table 4.5: Performance metrics for tire steering and pivot steering using the MPC.

(a) Rise times for $v_{x,cm}^v$ and δ_F, and maximum velocity tracking error during turning for the different steering configurations.

Steering configuration	$t_{r,v}$ (s)	$t_{r,\delta}$ (s)	$e_{v,max}^{(turn)}$ (m/s)
Tire steering	1.4507	0.8000	0.0584
Pivot steering	1.6320	0.6662	0.0672

(b) RMSE value for $v_{x,cm}^v$, δ_F and δ_R, and RMS value for τ_{tot} for the two steering configurations.

Steering configuration	v_{RMSE} (m/s)	δ_{FRMSE} (rad)	δ_{RRMSE} (rad)	τ_{RMS} (N/m^2)
Tire steering	0.1721	0.0385	0.0385	2930
Pivot steering	0.1725	0.0408	0.0409	2810

4.2.3 PI Tuning

The Figures in 4.5 displays the generated total shear stress for each wheel during the tuning test with the PI controller for both tire and pivot steering. It can be noted that the peak during the initial acceleration is sharper compared to the other controllers.

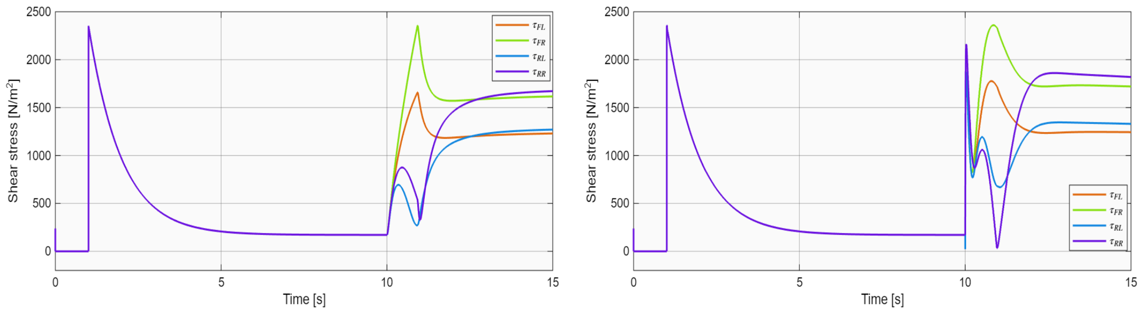

(a) Tire steering configuration.

(b) Pivot steering configuration.

Figure 4.5: Shear stress τ for each tire during the PI tuning test for the tire steering and pivot steering configurations.

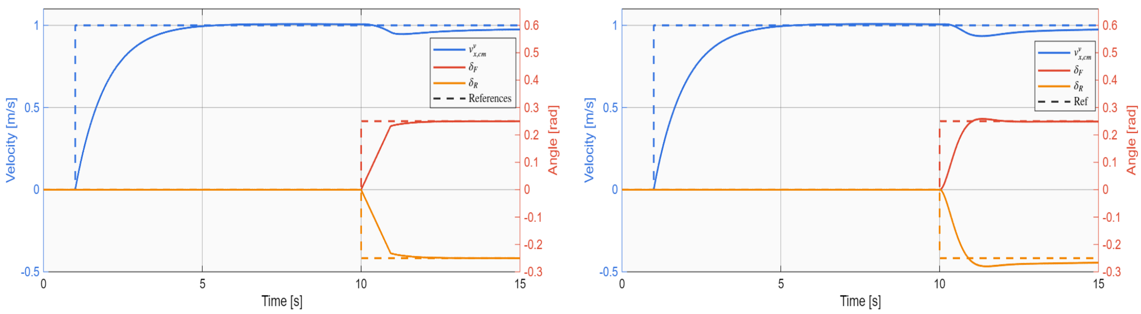

(a) Tire steering configuration.

(b) Pivot steering configuration.

Figure 4.6: Reference tracking of the longitudinal velocity v^x_{cm} and the steering angles δ_F and δ_R for the tire steering and pivot steering configurations using the tuned PI controller.

Table 4.6a and 4.6b shows the resulting rise time and RMS error for the PI controller during the tuning test as described in 3.6.3.2. The rise time for both the longitudinal velocity and the front steering angle is higher than for the other controllers.

Table 4.6: Performance metrics for tire steering and pivot steering using the PI controller.

(a) Rise times for $v^v_{x,cm}$ and δ_F, and maximum velocity tracking error during turning for the different steering configurations.

Steering configuration	$t_{r,v}$ (s)	$t_{r,\delta}$ (s)	$e^{(turn)}_{v,max}$ (m/s)
Pivot steering	2.0312	1.2109	0.0614
Tire steering	2.0315	0.8000	0.0535

(b) RMSE value for $v^v_{x,cm}$, δ_F and δ_R, and RMS value for τ_{tot} for the two steering configurations.

Steering configuration	RMSE v	RMSE δ_F	RMSE δ_R	RMS τ
Tire steering	0.1793	0.0376	0.0376	3018
Pivot steering	0.1796	0.0549	0.0552	2943

4.3 Asymmetric Terrain Conditions Test

The results below shows how the different controllers handle when two of the wheels are driving on a different type of ground for the two steering configurations, as described in Section 3.6.3.3.

4.3.1 Tire Steering

Figure 4.7 shows the reference tracking performance for the tire steering model using the PI, LQR and MPC controllers with the weights determined in Section 4.2.

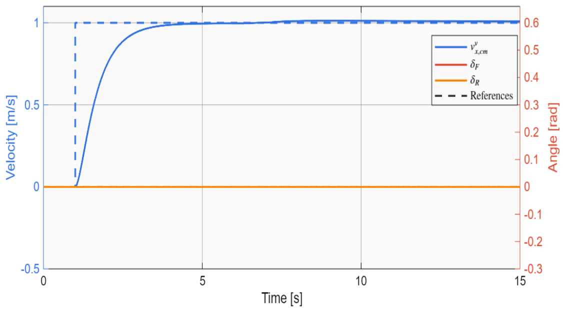

(a) LQR controller.

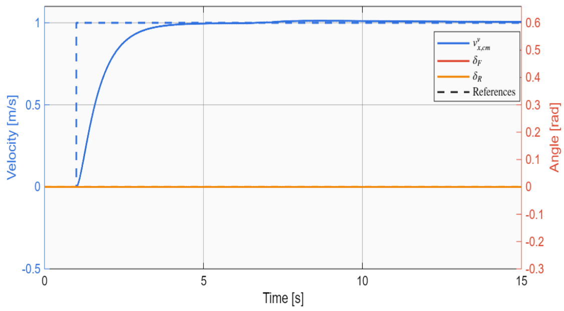

(b) MPC controller.

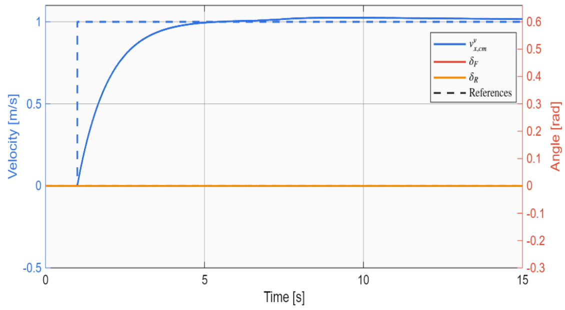

(c) PI controller.

Figure 4.7: Reference tracking of the longitudinal velocity $v^v_{x,cm}$ and steering angles δ_F and δ_R during the asymmetric terrain test for the tire steering configuration using the PI, LQR and MPC controllers.

Figure 4.8 shows the resulting shear stress τ at each tire using the PI, LQR and MPC controllers for tire steering. The shear stress settles at different values for the left- and right hand side tires.

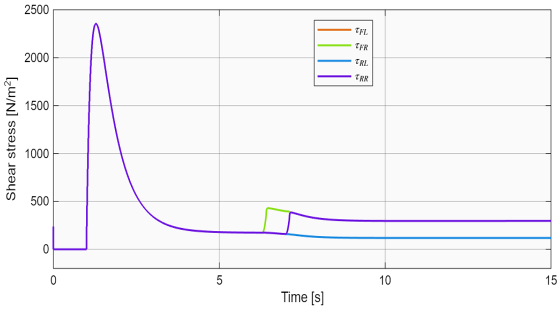

(a) LQR controller.

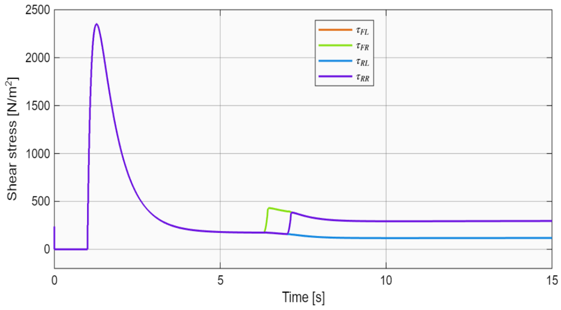

(b) MPC controller.

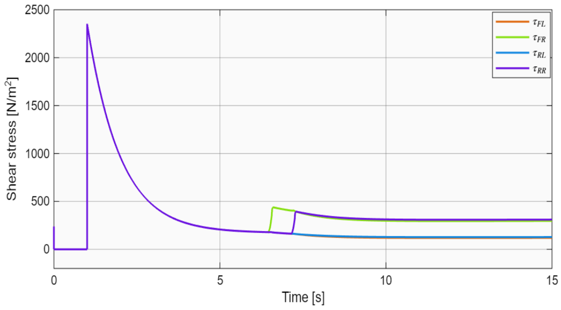

(c) PI controller.

Figure 4.8: Shear stress τ for each tire during the asymmetric terrain test for the tire steering configuration using the PI, LQR and MPC controllers.

Table 4.7 shows the RMSE values for $v^v_{x,cm}$, δ_F and δ_R, as well as the RMS value for τ_{tot}. It can be seen that the steering angles are not affected by the terrain change. The LQR and MPC controllers demonstrate comparable performance whereas the PI controller yields higher values for v_{RMSE} and τ_{RMS}.

Table 4.7: RMSE value for $v^v_{x,cm}$, δ_F and δ_R, and RMS value for τ_{tot} for tire steering using the LQR, MPC and PI controllers for the asymmetric terrain test.

Controller	v_{RMSE} (m/s)	δ_{FRMSE} (rad)	δ_{RRMSE} (rad)	τ_{RMS} (N/m^2)
LQR	0.1713	0.0000	0.0000	1297
MPC	0.1713	0.0000	0.0000	1294
PI	0.1788	0.0000	0.0000	1426

4.3.2 Pivot Steering

Figure 4.9 shows the reference tracking performance for the pivot steering model using the LQR and MPC controllers with the weights determined in 4.2. It can be observed that the steering angles settle with a steady state error after the vehicle enters the asymmetric terrain.

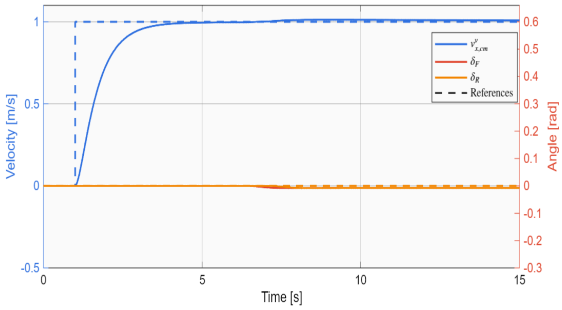

(a) LQR controller

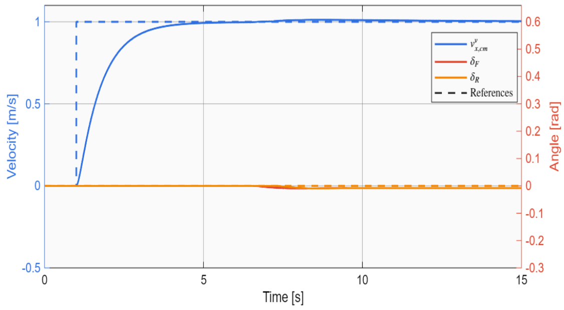

(b) MPC controller.

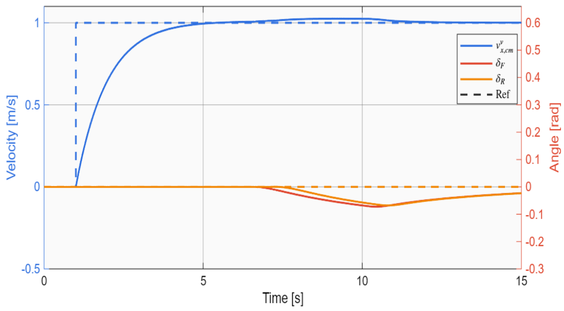

(c) PI controller.

Figure 4.9: Reference tracking of the longitudinal velocity $v^v_{x,cm}$ and steering angles δ_F and δ_R during the asymmetric terrain test for the pivot steering configuration using the PI, LQR and MPC controllers.

Figure 4.10 shows the shear stress τ for each tire using the PI, LQR and MPC controllers for pivot steering. The shear stress settles at closer values for the left and right hand side tires than for the tire steering configuration.

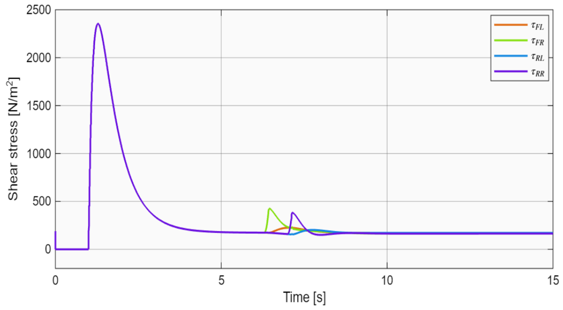

(a) LQR controller

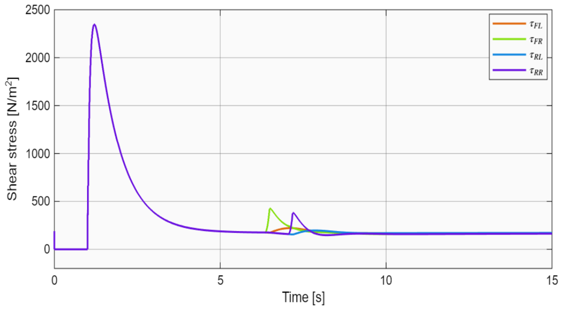

(b) MPC controller.

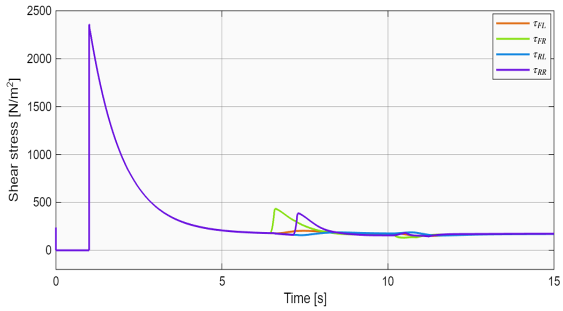

(c) PI controller.

Figure 4.10: Shear stress τ for each tire during the asymmetric terrain test for the pivot steering configuration using the PI, LQR and MPC controllers.

Table 4.8 shows the RMSE value for $v^v_{x,cm}$, δ_F and δ_R, as well as the RMS value for τ_{tot}. Unlike for tire steering, the steering angles are affected by the change of terrain, with non-zero values for δ_{FRMSE} and δ_{RRMSE}. It can also be noted that the values for τ_{RMS} are lower for all three controllers compared to the tire steering case in Table 4.7. Once again, the LQR and MPC controllers perform comparably while the PI controller results in higher tracking errors and RMS value for the total shear stress.

Table 4.8: RMSE value for $v^v_{x,cm}$, δ_F and δ_R, and RMS value for τ_{tot} for pivot steering using the LQR, MPC and PI controllers for the asymmetric terrain test.

Controller	v_{RMSE} (m/s)	δ_{FRMSE} (rad)	δ_{RRMSE} (rad)	τ_{RMS} (N/m^2)
LQR	0.1713	0.0053	0.0051	1210
MPC	0.1715	0.0057	0.0055	1206
PI	0.1788	0.0210	0.0200	1228

4.4 Slip Weights Test

The tables below shows ground impact and performance metrics with different non-zero weights on the slip ratio λ and slip angle β on all tires for the two steering configurations using the LQR and MPC controller.

4.4.1 Tire Steering

Table 4.9a shows the peak values reached for the slip ratio, λ_{peak}, slip angle, β_{peak}, and shear stress, τ_{peak}, for different weights on slip ratio and slip angle using the LQR controller for tire steering. Increased weights result in a lower value for λ_{peak}. The same does not hold for for the slip angle, where weights set to 5000 results in a higher value for β_{peak} than weights set to 500 or 2500. Table 4.9b shows the values for v_{RMSE}, δ_{FRMSE}, δ_{RRMSE} and τ_{RMS} where it can be observed that all values increase with higher weights on slip ratio and slip angle.

Table 4.9: Ground impact and performance metrics for weights on slip ratio and slip angle set to 500, 2500 and 5000 using the LQR controller for tire steering.

(a) Peak values for slip ratio λ, slip angle β and shear stress τ for different weights on slip ratio and slip angle for tire steering. The peak value for τ is reported for the acceleration and turning phase.

Weights	λ_{peak}	β_{peak} (rad)	$\tau_{peak}^{(acc)}$ (N/m^2)	$\tau_{peak}^{(turn)}$ (N/m^2)
500	0.1282	0.1223	2353	2358
2500	0.1016	0.1212	2118	2414
5000	0.0915	0.1449	1949	2826

(b) RMSE value for $v_{x,cm}^{v}$, δ_F and δ_R, and RMS value for τ_{tot} for different weights on slip ratio and slip angle.

Weights	v_{RMSE} (m/s)	δ_{FRMSE} (rad)	δ_{RRMSE} (rad)	τ_{RMS} (N/m^2)
500	0.1743	0.0380	0.0376	3052
2500	0.1814	0.0444	0.0405	3570
5000	0.1894	0.0559	0.0482	3980

Table 4.10a shows the peak values reached for the slip ratio, slip angle and shear stress for different weights on slip ratio and slip angle, using the MPC controller for tire steering. Increasing the weights result in a lower value for both λ_{peak} and β_{peak}. Table 4.10b shows the values for v_{RMSE}, δ_{FRMSE}, δ_{RRMSE} and τ_{RMS}. It can be observed that the RMSE values increase with higher weights while τ_{RMS} decreases.

Table 4.10: Ground impact and performance metrics for weights on slip ratio and slip angle set to 500, 2500 and 5000 on each tire using the MPC controller for tire steering.

(a) Peak values for λ, β and τ for different weights on slip ratio and slip angle for tire steering. The peak for τ is reported for the acceleration and turning phase.

Weights	λ_{peak}	β_{peak} (rad)	$\tau_{peak}^{(acc)}$ (N/m^2)	$\tau_{peak}^{(turn)}$ (N/m^2)
500	0.0943	0.1145	2001	2029
2500	0.0530	0.0960	1262	1912
5000	0.0331	0.0792	874	1610

(b) RMSE value for $v_{x,cm}^{v}$, δ_F and δ_R, and RMS value for τ_{tot} for different weights on slip ratio and slip angle.

weights	v_{RMSE} (m/s)	δ_{FRMSE} (rad)	δ_{RRMSE} (rad)	τ_{RMS} (N/m^2)
500	0.1873	0.0400	0.0382	2882
2500	0.2395	0.0498	0.0378	2772
5000	0.2911	0.0654	0.0391	2722

4.4.2 Pivot Steering

Table 4.11a shows the peak values reached for the slip ratio, slip angle and shear stress for different weights on slip ratio and slip angle, using the LQR controller for pivot steering. Similarly to tire steering, increased weights result in a lower value for λ_{peak} but a higher value for β_{peak}. Table 4.11b shows the values for v_{RMSE}, δ_{FRMSE}, δ_{RRMSE} and τ_{RMS}. It can be observed that all values increase with higher weights, as for tire steering.

Table 4.11: Ground impact and performance metrics for weights on slip ratio and slip angle set to 500, 2500 and 5000 on each tire using the LQR controller for pivot steering.

(a) Peak values for λ, β and τ for different weights on slip ratio and slip angle for pivot steering. The peak for τ is reported for the acceleration and turning phase.

Weights	λ_{peak}	β_{peak} (rad)	$\tau_{peak}^{(acc)}$ (N/m^2)	$\tau_{peak}^{(turn)}$ (N/m^2)
500	0.1129	0.1285	2299	2507
2500	0.1018	0.1513	2118	2879
5000	0.0915	0.1696	1949	3150

(b) RMSE value for $v_{x,cm}^{v}$, δ_F and δ_R, and RMS value for τ_{tot} for different weights on slip ratio and slip angle.

Weights	v_{RMSE} (m/s)	δ_{FRMSE} (rad)	δ_{RRMSE} (rad)	τ_{RMS} (N/m^2)
500	0.1749	0.0409	0.0412	2811
2500	0.1828	0.0481	0.0439	2898
5000	0.1912	0.0630	0.0522	2950

Table 4.12a shows the peak values reached using the MPC controller for pivot steering. Similarly to the MPC controller for tire steering, increasing the weights results in a lower value for both λ_{peak} and β_{peak}. Table 4.12b shows the values for v_{RMSE}, δ_{FRMSE}, δ_{RRMSE} and τ_{RMS}. The RMSE values increase with higher weights while τ_{RMS} decreases.

Table 4.12: Ground impact and performance metrics for weights on slip ratio and slip angle set to 500, 2500 and 5000 using the MPC controller for pivot steering.

(a) Peak values for λ, β and τ for different weights on slip ratio and slip angle for pivot steering. The peak for τ is reported for the acceleration and turning phase.

Weights	λ_{peak}	β_{peak} (rad)	$\tau_{peak}^{(acc)}$ (N/m^2)	$\tau_{peak}^{(turn)}$ (N/m^2)
500	0.1007	0.1189	2092	2332
2500	0.0635	0.1157	1448	2271
5000	0.0513	0.1138	1060	2232

(b) RMSE value for $v^v_{x,cm}$, δ_F and δ_R, and RMS value for τ_{tot} for different weights on slip ratio and slip angle.

weights	v_{RMSE} (m/s)	δ_{FRMSE} (rad)	δ_{RRMSE} (rad)	τ_{RMS} (N/m^2)
500	0.1836	0.0410	0.0411	2795
2500	0.2220	0.0419	0.0418	2755
5000	0.2602	0.0435	0.0427	2749

4.5 MPC Constraints Test

Table 4.13 shows the values for λ_{peak} and β_{peak} for tire steering and pivot steering for the unconstrained case in Section 4.2.2.

Table 4.13: Peak values for slip ratio λ and slip angle β for tire steering and pivot steering with no constraints.

Steering configuration	λ constraint	λ_{peak}	β constraint (rad)	β_{peak} (rad)
Tire steering	–	0.1162	–	0.1219
Pivot steering	–	0.1175	–	0.1200

Tables 4.14 and 4.15 shows the values for λ_{peak}, β_{peak}, $\tau_{peak}^{(acc)}$ and $\tau_{peak}^{(turn)}$ for tire and pivot steering with constraints set to 0.08 on each tire for both slip ratio and slip angle. For reference, the values for $\tau_{peak}^{(acc)}$ and $\tau_{peak}^{(turn)}$ were 2357 N/m^2 for the unconstrained case, as required in the tuning process. As shown, the constraints result in lower peak values for tire slip and consequently for the shear stress.

Table 4.14: Peak values for λ and β when constrained to 0.08.

Steering configuration	λ constraint	λ_{peak}	β constraint (rad)	β_{peak} (rad)
Tire steering	0.08	0.0638	0.08	0.1008
Pivot steering	0.08	0.0637	0.08	0.0899

Table 4.15: Peak values for τ during the acceleration and turning phase with constraints on λ and β.

Steering configuration	$\tau_{peak}^{(acc)}$ (N/m^2)	$\tau_{peak}^{(turn)}$ (N/m^2)
Tire steering	1463	1996
Pivot steering	1459	1831

Figures 4.11a and 4.11b shows the reference tracking performance for tire steering and pivot steering with constraints on slip ratio and slip angle. For pivot steering, less overshooting can be observed for δ_F and δ_R compared to the unconstrained case.

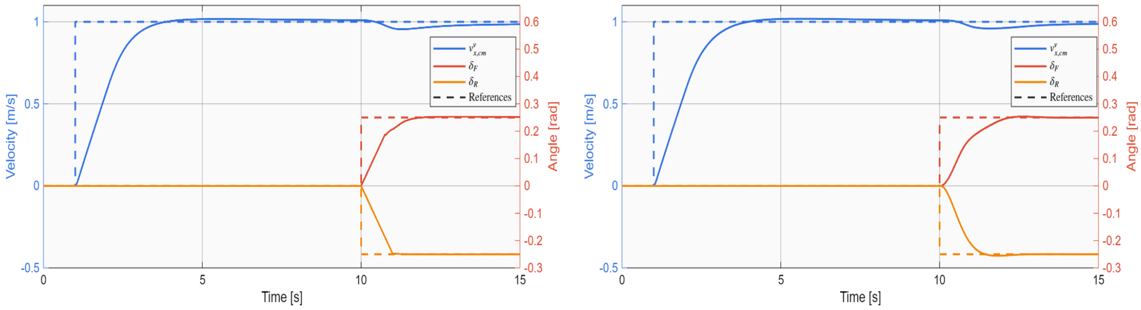

(a) Tire steering configuration. **(b)** Pivot steering configuration.

Figure 4.11: Reference tracking of the longitudinal velocity v^x_{cm} and the steering angles δ_F and δ_R for the tire steering and pivot steering configurations using the MPC controller with constraints on slip ratio λ and slip angle β.

Figure 4.12 shows the resulting shear stress τ for each tire for the tire steering and pivot steering model with constraints on slip ratio and slip angle. For the acceleration phase, it can be noted that the peak values reached a more flat value compared to the unconstrained case, shown in Figure 4.4.

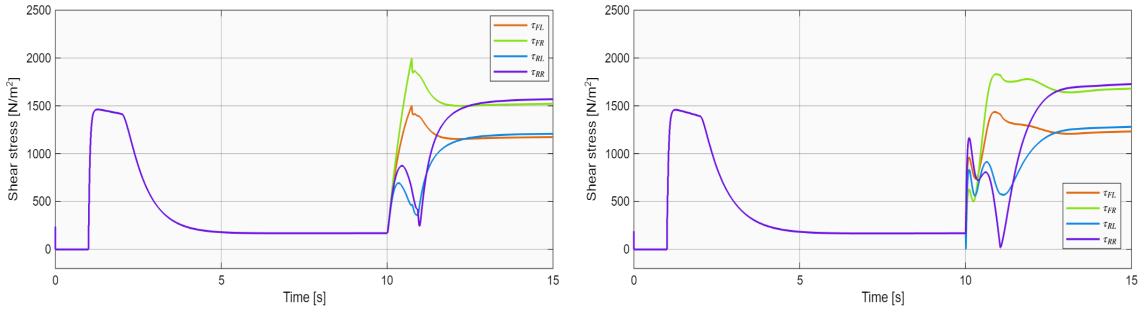

(a) Tire steering configuration. **(b)** Pivot steering configuration.

Figure 4.12: Shear stress τ for each tire for the tire steering and pivot steering configurations using the MPC with constraints on λ and β.

Table 4.16a shows the rise times $t_{r,v}$ and $t_{r,\delta}$ as well as $e_{v,max}^{(turn)}$ for pivot steering and tire steering using the MPC controller with constraints on λ and β. The values for $t_{r,v}$ and $t_{r,\delta}$ increase while the value for $e_{v,max}^{(turn)}$ decrease compared to the unconstrained case, shown in Table 4.5a. Table 4.16b shows the values for v_{RMSE}, δ_{FRMSE}, δ_{RRMSE} and τ_{RMS} for the constrained case.

Table 4.16: Performance metrics for the MPC controller using tire steering and pivot steering with slip ratio λ and slip angle β constrained.

(a) Rise times for $v^v_{x,cm}$ and δ_F, and maximum velocity tracking error during turning for the different steering configurations.

Steering configuration	$t_{r,v}$ (s)	$t_{r,\delta}$ (s)	$e^{(turn)}_{v,max}$ (m/s)
Tire steering	1.6190	1.280	0.0417
Pivot steering	1.6922	1.3850	0.0409

(b) RMSE value for $v^v_{x,cm}$, δ_F and δ_R, and RMS value for τ_{tot} for the two steering configurations.

Steering configuration	v_{RMSE} (m/s)	δ_{FRMSE} (rad)	δ_{RRMSE} (rad)	τ_{RMS} (N/m^2)
Tire steering	0.1998	0.0397	0.0385	3083
Pivot steering	0.2004	0.0474	0.0436	2694

4.6 EKF Test

Table 4.17 lists the RMSE values of the estimated states for both the tire and pivot steering model compared to the simulated states during the scenario described in Section 3.6.4. The error is relatively low for the non observed states and a bit higher for the observed states with added noise levels.

Table 4.17: RMSE values between the simulated and estimated states for the implemented EKF during acceleration and steering.

State	Tire steering RMSE	Pivot steering RMSE
v_x	0.0065	0.0069
v_y	0.0002	0.0020
$\dot{\psi}$	0.0143	0.0030
ω_1	0.1134	0.1273
ω_2	0.1833	0.1230
ω_3	0.1299	0.1238
ω_4	0.1676	0.1337
$\dot{\delta}_F$	–	0.0004
$\dot{\delta}_R$	–	0.0060
δ_F	0.0005	0.0001
δ_R	0.0005	0.0002

The performance of the LQR controller together with the EKF for state estimation is summarized in the Tables 4.18, 4.19 and 4.20. Both the steering configurations achieve a lower rise time using the implemented filter compared to using the simulated states as controller input. They also reach slightly higher peak shear stress as well.

Table 4.18: Rise times for $v^v_{x,cm}$ and δ_F, and maximum velocity tracking error during turning for the different steering configurations using the EKF and LQR.

Steering configuration	$t_{r,v}$ (s)	$t_{r,\delta}$ (s)	$e^{(turn)}_{v,max}$ (m/s)
Tire steering	1.3290	0.8100	0.0546
Pivot steering	1.3269	0.6121	0.0614

Table 4.19: RMSE during acceleration and steering with the implemented EKF and LQR.

Steering configuration	v_{RMSE} (m/s)	$\delta_{F\,RMSE}$ (rad)	$\delta_{R\,RMSE}$ (rad)	τ_{RMS} (N/m^2)
Tire steering	0.1703	0.0376	0.0376	$3.0855 \cdot 10^3$
Pivot steering	0.1698	0.0412	0.0412	$3.1895 \cdot 10^3$

Table 4.20: Peak values for τ during the acceleration and turning phase with the implemented EKF together with the LQR controller.

Steering configuration	$\tau^{(acc)}_{peak}$	$\tau^{(turn)}_{peak}$
Tire steering	2392	2390
Pivot steering	2410	3153

5

Discussion

5.1 Model Limitations and Inaccuracies

A simplified model is used for the simulation, which introduces uncertainty regarding how well the results translate to a practical application. One limitation is that the wheel sinkage ratio Λ is unknown and set to an assumed value for the simulation. However, in reality it changes depending on the soil and type of surface the vehicle is driving on. If the value differs drastically from the simulation, the shear forces generated in reality could vary greatly from the simulation, making the developed controllers less applicable. Furthermore, dynamic sinkage is neglected for simplicity, as described in Section 3.6, which adds to the mismatch between simulation and reality.

The tests are carried out on a limited selection of soils, and it is therefore difficult to predict how it would behave on other types of soils. The soil is also modelled as a uniform material, without any deviation such as stones, or compact regions and can therefore not say anything about these scenarios. The tire model used is also a simplification as it does not model a decrease in shear forces after reaching a certain slip rate or angle but instead approaches a saturated maximum. However, this is not as relevant in this case as the tests are only performed in scenarios where slip rate and angle are well under these limits. Higher accuracy could potentially be achieved by using alternative soil and tire interaction models, such as particle-based or finite element methods, to model these variables in greater detail. Another modelling assumption is that the bulldozing force was only included as a lateral tire force, since the longitudinal contribution was assumed to be negligible for the driving cases considered and is more difficult to model accurately. It could however contribute more when driving on very loose terrain that could build up in front of the tires.

Another simplification is Simpson's 1/3 rule that is used to estimate the integrals 2.16 and 2.17. It gives a computationally efficient approximate value for the integrals but introduces some error. It is deemed reasonable to use since the stress distributions for the normal stress $\sigma(\theta)$ and shear stress $\tau(\theta)$ vary smoothly with the wheel angle θ. Therefore, the method is assumed to capture the overall behaviour of the stresses with just three evaluation points which reduces computational cost while still providing reliable estimates of the longitudinal and lateral tire forces. For the calculation of $F_{x,rot,i}$, the normal stress $\sigma(\theta)$ is not assumed to provide a rotational force for the tire. This is a simplification meaning that the vector for $\sigma(\theta)$ goes through the tire's rotational center for all θ. In reality this is not necessarily the case but is assumed for computational simplicity.

Because of the simplifications made for the simulation, the results should primarily be interpreted as a relative comparison between the different steering configurations and controller implementations under different circumstances rather than exact predictions of how the modelled vehicles and controllers will behave during physical implementation.

5.2 Steering Configurations Effect of Shear Stress

When it comes to the two steering mechanisms, pivot steering reduces the shear stresses $\tau_{x,tot}$ and $\tau_{y,tot}$ generated by the vehicle on the ground compared to tire steering, as seen in the Table 4.1. It also reduces τ_{RMS} during the asymmetric terrain test as seen in Tables 4.7 and 4.8. However, as seen in tables 4.3b, 4.5b and 4.6b, the pivot steering method consistently has larger steering angle tracking errors, δ_{FRMSE} and δ_{RRMSE}, than the tire steering configuration. For the asymmetric terrain test, Tables 4.7 and 4.8 show large differences in these values. The reason is that δ_F and δ_R settles with a steady state error during the asymmetric terrain phase. Based on the tuning results, it was deemed that integral action for steering was not required for any of the setups, but as shown it is required for the pivot steering model. This could simply be added to both the LQR and MPC controller. The steering angles for pivot steering also tend to overshoot slightly as seen in Figures 4.1b and 4.3b and consistently perform worse when it comes to controlling the steering angles with as high precision as the tire steering method. Table 4.1a, shows that there is a larger increase in the shear stress in x compared to in y, which indicates that the pivot steering method trades part of the lateral shear to longitudinal as the steering is not able to be changed aggressively without causing a higher longitudinal shear stress.

In Figures 4.8 and 4.10, the shear stress on the right hand side differs more for the tire steering configuration than for the pivot-steering configuration on asymmetric terrain. This is because the tire steering controller only controls the longitudinal velocity and steering angles, while the applied wheel torques are decoupled from the steering motion. As a result, approximately the same torque is applied to all four wheels regardless of terrain conditions, causing the right hand side wheels to generate higher shear stress when they enter the changed terrain. For the pivot-steering configuration, the steering angles are directly affected by the wheel torques. The controller therefore redistributes the torques to counteract the axle rotation caused by the asymmetric terrain and maintain the desired steering angle. This reduces the relative increase in shear stress on the righthand side, but instead increases the shear stress on the left hand side as compensation. For the tire steering model, the same limitation applies in general driving scenarios, since the wheel torques are not adjusted according to each wheel's distance from the turning centre, which has the additional consequence that the Ackermann steering mechanism will not work ideally. This can cause excessive tire slip and is a likely reason for the difference in generated shear stresses reported in 4.1. However, if the individual wheel angular velocities or the vehicle yaw rate were controlled, the tire steering configuration could potentially adapt through differential wheel torques in a similar way to the pivot steering configuration. This would require a redesign of the state space formulation.

5.3 Controller Analysis

The PI controller tuned for the same criterion for τ_{peak}^{acc} and τ_{peak}^{turn} as the LQR and MPC controllers has higher rise times for the velocity, $t_{r,v}$, as well as for the front steering angle, $t_{r,\delta}$, for pivot steering, as shown in Tables 4.3a, 4.5a and 4.6a. This is likely because of the smoother control inputs applied as a result of the input rate penalty incorporated in the cost function for the model based controllers. For tire steering, $t_{r,\delta}$ is identical for all three controllers. The reason is that the steering rate was limited by a fixed maximum value. As a result, the steering angle rise time becomes less relevant for comparing controller performance, since all controllers produce nearly identical steering responses once the rate limit is reached. A less restrictive rate constraint could have provided a clearer comparison between the controllers. However, the chosen limit was based on the physical vehicle model and was therefore kept consistent with the first-order steering delay used in the state-space representation.

The LQR and MPC controllers perform similarly for tire steering and pivot steering with the chosen N_p and N_c, as shown in Section 4.2. The rise time $t_{r,v}$ increase for the MPC controller compared to the LQR controller for both tire steering and pivot steering as shown in Tables 4.3a and 4.5a. For pivot steering, the increase is greater than for tire steering which is a result of the change in prediction horizon and different weights in Q_y and R_y required to fulfil the tuning criterion for $\tau_{\text{peak}}^{(turn)}$ The rise time $t_{r,\delta}$ also increases when using the MPC controller for the pivot steering model. For tire steering, there is no difference in $t_{r,\delta}$ because the maximal steering rate is reached for both the LQR and MPC controller. Because the controllers are only performing setpoint tracking with unknown future references, it is expected that the MPC solution will converge to the corresponding LQR solution with infinite horizons. Therefore, the MPC controller cannot exploit one of its principal advantages of anticipating known future reference trajectories. The integral action is implemented differently for the LQR and MPC controller and therefore the values for v_{RMSE}, $\delta_{R_{RMSE}}$, $\delta_{R_{RMSE}}$ and τ_{RMS} in Tables 4.3b and 4.5b cannot be compared directly but it may be assumed that the reference tracking capabilities are better for the LQR controller because of its optimal feedback gain. The main benefits of using the MPC controller becomes apparent in the tests described in Sections 3.6.3.4 and 3.6.3.5, as discussed further below.

Both the LQR and MPC controllers behave as desired when setting weights on the slip ratio λ, with higher weights resulting in lower values for λ_{peak} and $\tau_{peak}^{(acc)}$ on all tires, as shown in Tables 4.9a, 4.10a, 4.11a and 4.12a. Setting weights on the slip angle β results in different behaviour for the LQR and MPC controller. Higher weights resulted in a higher value for β_{peak} when using the LQR controller whereas it resulted in a lower value when using the MPC controller. This result is consistent for both tire steering and pivot steering. One potential explanation is that the MPC controller benefits from its shorter horizon in this case. The LQR controller computes a feedback gain by minimizing an infinite-horizon cost function, which results in a control law that prioritizes overall long-term performance. In contrast, the MPC controller optimizes over a finite prediction horizon and therefore places greater emphasis on short-term transient behaviour. Since the peak in β occurs over a relatively short time interval, the MPC controller is better able to actively suppress this transient peak, while the LQR controller may instead accept a temporary increase in β in order to improve the overall trajectory. Tables 4.9b, 4.10b, 4.11b and 4.12b show that the values for v_{RMSE}, δ_{FRMSE} and δ_{RRMSE} generally increase with higher weights on the slip ratio and slip angle for both steering and controller setups, which is expected because the solution to the optimization problem prioritizes reduced slip at the cost of reference tracking performance. The value of τ_{RMS} increases for the LQR controller and decreases for the MPC.

The MPC controller was able to incorporate output constraints on slip ratio and slip angle as shown in Section 4.5. The constraints resulted in lower values for λ_{peak} and β_{peak} for both tire steering and pivot steering, as shown in Table 4.14, although it was not able to keep the exact constraints that were set. Because of the soft constraints used it is expected that the outputs may surpass the constraints, as observed for β. Potential reasons for λ_{peak} settling below the constraint could be a model mismatch between the non-linear vehicle system and the linearized state space formulation or insufficient prediction horizon. Figure 4.12 shows that the shear stress τ for each tire reaches lower values compared to the unconstrained case in Figure 4.4. In particular, it can be noted that during acceleration, τ has a flatter peak values instead of sharp transient peaks, which is beneficial for reducing excessive ground impact while still maintaining high reference tracking performance. Tables 4.5a and 4.16a show that the rise times $t_{r,v}$ and $t_{r,\delta}$ increase for the constrained case compared to the unconstrained case. Notably, for tire steering, an increase in $t_{r,v}$ of 11.6% is accompanied by a reduction in $\tau_{peak}^{(acc)}$ of 37.9%. Similarly, for pivot steering, a 3.7% increase in $t_{r,v}$ results in a 38.1% reduction in $\tau_{peak}^{(acc)}$. Thus, a relatively high reduction in ground impact is achieved at the cost of a relatively low impact on performance in this case. Another benefit of the MPC controller is that it allows for input constraints on the applied torque as well. For tire steering, constraints can also be set for the steering angles. While only the soft output constraints were explicitly evaluated, the hard input constraints are enforced directly by the optimizer and are therefore guaranteed to be satisfied for any feasible MPC solution.

A detailed execution time analysis was not performed for the LQR or MPC controller during simulation, as simulation results do not reflect the actual hardware. While the controller consistently stayed below the sampling rate of 10 ms during testing, these results were influenced by the simulation computer's performance rather than the target embedded processor. Therefore, these figures were used as a feasibility check rather than as a final measure of real-time performance. Although the MPC showed promising result, implementing a high frequency MPC could be difficult on a physical system because of the high computational cost. It is however suspected that a high sampling rate is needed for the MPC to be able to handle the constraints efficiently as the slip dynamics can change rapidly. In contrast, LQR is less demanding and could therefore be more suitable for real time implementation. Further test of the controller sampling time should therefore be investigated regarding how it effects the controllers ability to regulate the slip ratio and slip angle as a lower sampled MPC could be more realistic. A development potential for the MPC is to add terminal weights to the cost function

A possible development of the MPC is to add a terminal cost on the final predicted output deviation. This terminal cost could be designed using a Riccati equation, and in a more complete formulation it could also account for the input-rate penalty by augmenting the system with the previous input. The purpose of a terminal cost is to encourage the optimizer to end the prediction horizon in a state from which continued regulation is inexpensive. This may allow for a shorter prediction horizon to be used while maintaining similar closed-loop performance, which is especially relevant for hardware implementation as it would lower the execution time.

The extended Kalman filter seems to be able to estimate the non measured states and remove most of the measurement noise in both of the steering configurations as seen in Table 4.17. Further improvement could possibly be made with better tuning of the filter parameters. It can be observed in 4.18 that there is a decrease in rise time for both the longitudinal velocity and steering angles compared to when simulated states are used for the controller in 4.3a. This is likely because of the deviation in the state estimation, resulting in the initial tuning overshooting the limit of 25% of the soils maximal shear stress. Table 4.20 shows the resulting stress higher than the 25% limit. As a result, the controller becomes more aggressive, resulting in a higher peak acceleration.

5.4 Future Work

This work has analysed how different model based control methods could benefit the reduction in ground tear, but it still lacks the ability to fully compensate and adjust the control input with the changes in ground parameters. It would therefore be of interest to estimate these parameters live on the vehicle in order to adjust the control action to better suit the ground type. This could potentially be done with a simple rule based classification or online parameter estimation with an EKF, where the state vector is expanded with unknown slow changing parameters. This could then be used together with gain scheduling for the LQR controller and MPC.

A more in depth sensitivity analysis should also be performed to evaluate the robustness of the controller against model uncertainties. This could include changes in miss match in controller model parameter and the physical system, variations in the vehicles mass or more extreme changes in terrain conditions. This would give better understanding on how dependent the controllers are on accurate model parameters.

Future work should also include physical implementation of the developed controllers. This would make it possible to evaluate the computational feasibility of both the LQR, but most importantly the MPC and whether the simulated performance can be achieved in practice. Such an implementation would also allow for a more detailed investigation of the sampling time and the choice of control and prediction horizons for the MPC. In addition, experimental testing could be used to evaluate both the runtime performance of the controllers and the generated shear forces under real operating conditions.

6
Conclusion

This study has analysed how two different steering methods, tire steering and pivot steering, can be utilized together with model based control methods for reference tracking of the longitudinal velocity, and front and rear steering angles, with the ultimate goal of minimizing the vehicle's ground impact. An LQR and MPC controller was developed with weighting capabilities on slip ratio and slip angle, since these are directly related to the shear forces between the vehicle tires and the ground. Furthermore, the controllers were developed with the ability to incorporate input rate penalties in order to penalize rapid changes in the controller input, allowing for incremented increases in control effort which reduce sudden changes in tire forces.

To evaluate the steering methods and controller, the tire and ground interaction was modelled and implemented for both steering methods in Simulink and Simscape. The controllers were tuned for a selected ground type to achieve a peak shear stress of 25% of the maximum shear stress the ground can withstand. Several simulation tests were then performed and the results were compared to a traditional PI controller. The results show that the pivot-steering configuration can reduce the total generated shear forces while achieving a similar yaw rate during turns compared to the tire steering configuration. Under asymmetric terrain conditions, the pivot steering configuration also results in a lower total shear force. However, this reduction is not necessarily associated with improved overall performance, since the steering angle tracking performance is reduced slightly as the angles often overshoot their references.

Both LQR and MPC improved the longitudinal acceleration while maintaining the shear stress limitation compared to the PI controller, likely due to the input increment implementation. Increasing the weight on slip ratio reduced the longitudional shear stress for both controllers. However, only the MPC was able to reduce the lateral shear through the introduction of cost on the slip angle. The MPC was also able to implement soft constraints on both the slip ratio and slip angle with promising results. The slip angle was nevertheless more difficult to regulate than the slip ratio.

Overall, the results indicate that both the selection of steering method and controller has significant influence on the generated shear. Pivot steering along with the MPC controller showed the greatest potential when it comes to reducing ground shear forces as it is also capable at handling constraints.

Bibliography

[1] G. Ishigami, A. Miwa, K. Nagatani and K. Yoshida, "Terramechanics-based model for steering maneuver of planetary exploration rovers on loose soil," *Journal of Field Robotics*, vol. 24, No.3, pp. 233–250, Mar. 2007. [online] Available: `doi.org/10.1002/rob.20187`.

[2] K. Yoshida, T. Watanabe, N. Mizuno and G. Ishigami, "Terramechanics-Based Analysis and Traction Control of a Lunar/Planetary Rover," in *Proceedings of the International Conference on Field and Service Robotics*, Yamanashi, Japan, 2003, pp. 225–234. [Online]. Available: `https://doi.org/10.1007/10991459_22`.

[3] J. Y. Wong, *Theory of ground vehicles*. 4th. Ed., Ottawa, Canada: John Wiley & Sons, Inc, 2008.

[4] K. Yoshida and G. Ishigami, "Steering Characteristics of a Rigid Wheel for Exploration on Loose Soil" in *Proceedings of the International Conference on Intelligent Robots and Systems*, Sendai, Japan, 2004, pp. 3995-4000. [Online]. Available: `https://ieeexplore.ieee.org/document/1390039`.

[5] E. Hegedus, "A Simplified Method for the Determination of Bulldozing Resistance," Land Locomotion Laboratory, Research Division, Research and Engineering Directorate, Detroit Arsenal, Center Line, MI, USA, Report No. RR-22, 1960.

[6] G. F. Franklin, J. D. Powell, and M. L. Workman, *Digital Control of Dynamic Systems*, 3rd ed. Reading, MA, USA: Addison-Wesley, 1998.

[7] B. Lennartsson, *Reglerteknikens grunder*. 4th ed., Lund, Sweden, Studentlitteratur AB, 2002.

[8] T. Glad, L, Ljung, *Control theory: Multivariable and Nonlinear methods*. 1st Ed, London, England, Taylor & Francis, 2000.

[9] Schwenzer, Max and Ay, Murat and Bergs, Thomas and Abel, Dirk, "Review on Model Predictive Control: An Engineering Perspective", The International Journal of Advanced Manufacturing Technology, vol. 117, pp. 1327-1349, Aug 2021, [Online] Available: `10.1007/s00170-021-07682-3`.

[10] G. Welch and G. Bishop, "An Introduction to the Kalman Filter," Dept. Comput. Sci., Univ. North Carolina Chapel Hill, Chapel Hill, NC, USA, Tech. Rep. TR 95-041, 2004. [Online] Available: `https://techreports.cs.unc.edu/papers/95-041.pdf`

[11] R. A. Adams and C. Essex, *Calculus: A Complete Course*. 9th ed., Toronto, Canada: Pearson Addison Wesley, 2018.

[12] Gillespie, T. *Fundamentals of Vehicle Dynamics, Revised Edition*, Warrendale, PA, USA, SAE International, 2021. [online] Avaliable: `https://doi.org/10.4271/R-506`

[13] P. Jansson, R. Grahn, M. Enelund, *Mekanik: Statik och Dynamik.* 4th Ed., Lund, Sweden, Studentlitteratur AB, 2018.

[14] A. E. Bryson, Jr. and Y.-C. Ho, *Applied Optimal Control: Optimization, Estimation, and Control*, rev. printing., New York, NY, USA: Taylor & Francis Group, 1975.

A

Appendix 1

A.1 LQR feedforward derivation

For reference tracking, the steady-state values (x_{ss}) and (u_{ss}) were computed from the discrete-time state-space model

$$x(k+1) = A_d x(k) + B_d u(k).$$

At steady state, the state is constant, which gives

$$x_{ss} = A_d x_{ss} + B_d u_{ss}.$$

Rearranging gives

$$(I - A_d)x_{ss} = B_d u_{ss},$$

and therefore

$$x_{ss} = (I - A_d)^{-1} B_d u_{ss}.$$

The controlled output is defined as

$$y = Cx.$$

Since the desired steady-state output should satisfy $y_{ss} = y_{ref}$, the following relation is obtained:

$$y_{ref} = Cx_{ss}.$$

Substituting the expression for x_{ss} gives

$$y_{ref} = C(I - A_d)^{-1} B_d u_{ss}.$$

The steady-state input can therefore be written as

$$u_{ss} = K_{ur} y_{ref},$$

where

$$\left(C(I - A_d)^{-1} B_d\right)^{\dagger}.$$

Since the matrix $(C(I - A_d)^{-1}B_d)$ is not square in the implemented models, the Moore Penrose pseudoinverse was used. The corresponding steady-state state vector is then

$$x_{ss} = K_{xr} y_{ref},$$

where

$$(I - A_d)^{-1} B_d K_{ur}.$$

A.2 MPC derivations

This appendix presents the detailed matrix formulation used for the condensed MPC implementation described in Section 3.4.2. To formulate the optimization problem in compact matrix form, block diagonal weighting matrices are constructed over the prediction horizon. The lifted output weighting matrix is defined as

$$\bar{Q}_y = \text{blkdiag}(Q_y, \ldots, Q_y).$$

Similarly, the lifted input weighting matrix is defined as

$$\bar{R} = \text{blkdiag}(R_u, \ldots, R_u).$$

and the lifted input rate weighting matrix is defined as

$$\bar{R}_{\Delta u} = \text{blkdiag}(R_{\Delta u}, \ldots, R_{\Delta u}).$$

These matrices penalize the predicted output tracking errors, control effort, and the variation in the control inputs over the prediction horizon. The prediction model used in the condensed MPC formulation is then constructed. Instead of treating the predicted states as optimization variables, the future states are expressed explicitly as functions of the initial state and the future control sequence. The stacked future state vector is defined as

$$X = \begin{bmatrix} x(1) \\ x(2) \\ \vdots \\ x(N_p) \end{bmatrix}$$

and the stacked control sequence over the control horizon is defined as

$$U_c = \begin{bmatrix} u(0) \\ u(1) \\ \vdots \\ u(N_c - 1) \end{bmatrix}.$$

Using repeated substitution of the system dynamics, the future state trajectory can be written compactly as

$$X = \Omega x_0 + \Gamma U$$

where Ω is the free response prediction matrix and Γ is the forced response prediction matrix. The matrix Ω contains the autonomous evolution of the system and is constructed as

$$\Omega = \begin{bmatrix} A_d \\ A_d^2 \\ \vdots \\ A_d^{N_p} \end{bmatrix}.$$

The matrix Γ describes how future control inputs influence future states and has the lower block triangular structure

$$\Gamma = \begin{bmatrix} B_d & 0 & 0 & \cdots & 0 \\ A_d B_d & B_d & 0 & \cdots & 0 \\ A_d^2 B_d & A_d B_d & B_d & \cdots & 0 \\ \vdots & \vdots & \vdots & \ddots & \vdots \\ A_d^{N_p-1} B_d & A_d^{N_p-2} B_d & A_d^{N_p-3} B_d & \cdots & B_d \end{bmatrix}.$$

The predicted outputs are then constructed by stacking all future outputs into the vector

$$Y = \begin{bmatrix} y(1) \\ y(2) \\ \vdots \\ y(N_p) \end{bmatrix}.$$

To obtain a compact output prediction equation, block diagonal matrices containing the output matrices are introduced as

$$\hat{C} = I_{N_p} \otimes C_d$$

$$\hat{D} = I_{N_p} \otimes D_d$$

where $\otimes$ denotes the Kronecker product. Using the previously derived state prediction equation, the predicted outputs can be written as

$$Y = \hat{C} X + \hat{D} U$$

and substituting the state prediction equation yields

$$Y = \hat{C}(\Omega x_0 + \Gamma U) + \hat{D} U.$$

To reduce the number of optimization variables and improve computational efficiency, the future control inputs are only optimized over the control horizon N_c. For prediction steps beyond the control horizon, the final optimized control input is held constant. This is implemented using the mapping

$$U = SU_c$$

where S is a block selection matrix mapping the reduced control sequence U_c to the full prediction horizon input sequence U. The condensed output prediction equation can therefore be written as

$$Y = Fx_0 + \Phi_u U_c$$

where

$$F = \hat{C}\Omega$$

and

$$\Phi_u = \Phi_{\text{full}} S$$

with

$$\Phi_{\text{full}} = \hat{C}\Gamma + \hat{D}.$$

The condensed formulation eliminates the predicted states from the optimization problem and expresses the future outputs solely as functions of the current state and future control sequence. To penalize the rate of change of the control input, the stacked control increment vector is defined as

$$\Delta U = \begin{bmatrix} u(0) - u(-1) \\ u(1) - u(0) \\ u(2) - u(1) \\ \vdots \\ u(N_c - 1) - u(N_c - 2) \end{bmatrix}$$

where $u(-1)$ denotes the previously applied control input. The stacked input increments can be expressed compactly as

$$\Delta U = TU_c + d$$

where T is the lower bidiagonal difference matrix

$$T = \begin{bmatrix} I & 0 & 0 & \cdots & 0 \\ -I & I & 0 & \cdots & 0 \\ 0 & -I & I & \cdots & 0 \\ \vdots & \vdots & \vdots & \ddots & \vdots \\ 0 & 0 & 0 & -I & I \end{bmatrix}$$

and the offset vector d is defined as

$$d = \begin{bmatrix} -u(-1) \\ 0 \\ \vdots \\ 0 \end{bmatrix}.$$

The finite horizon cost function can now be rewritten in compact matrix form as

$$J = (Y - R)^T \bar{Q}_y (Y - R) + U_c^T \bar{R} U_c + (TU_c + d)^T \bar{R}_{\Delta u} (TU_c + d) + \rho_\epsilon \epsilon^2.$$

where R is the stacked reference vector

$$R = \begin{bmatrix} y_{ref} \\ y_{ref} \\ \vdots \\ y_{ref} \end{bmatrix}.$$

Substituting the condensed output prediction equation into the cost function gives

$$J = (Fx_0 + \Phi_u U_c - R)^T \bar{Q}_y (Fx_0 + \Phi_u U_c - R) + U_c^T \bar{R} U_c + (TU_c + d)^T \bar{R}_{\Delta u} (TU_c + d) + \rho_\epsilon \epsilon^2.$$

Expanding the quadratic expression results in

$$J = U_c^T \left(\Phi_u^T \bar{Q}_y \Phi_u + \bar{R} + T^T \bar{R}_{\Delta u} T \right) U_c + 2(Fx_0 - R)^T \bar{Q}_y \Phi_u U_c + 2d^T \bar{R}_{\Delta u} T U_c + \rho_\epsilon \epsilon^2 + \text{constant}.$$

Since the constant term does not affect the optimization, it is omitted. The optimization problem is then converted into the standard quadratic programming form used by Matlab's `quadprog` solver. The optimization vector is augmented with the slack variable according to

$$z = \begin{bmatrix} U_c \\ \epsilon \end{bmatrix}.$$

The Hessian matrix is therefore defined as

$$H = \begin{bmatrix} H_u & 0 \\ 0 & 2\rho_\epsilon \end{bmatrix}$$

where

$$H_u = 2 \left(\Phi_u^T \bar{Q}_y \Phi_u + \bar{R} + T^T \bar{R}_{\Delta u} T \right)$$

and the gradient vector is defined as

$$f = \begin{bmatrix} 2\Phi_u^T \bar{Q}_y (Fx_0 - R) + 2T^T \bar{R}_{\Delta u} d \\ 0 \end{bmatrix}.$$

Input constraints are incorporated as hard linear inequality constraints. Upper and lower bounds on the control inputs are defined as

$$u_{\min} \leq u(k) \leq u_{\max}, \quad k = 0, \ldots, N_c - 1$$

These constraints are rewritten as

$$\begin{bmatrix} I \\ -I \end{bmatrix} u(k) \leq \begin{bmatrix} u_{\max} \\ -u_{\min} \end{bmatrix}$$

and stacked across the control horizon as

$$\left(I_{N_c} \otimes \begin{bmatrix} I \\ -I \end{bmatrix} \right) U_c \leq \mathbf{1}_{N_c} \otimes \begin{bmatrix} u_{\max} \\ -u_{\min} \end{bmatrix}.$$

In addition to input constraints, constraints are imposed on selected predicted outputs. To improve robustness and avoid overly aggressive behaviour near the constraint boundaries, the output constraints are implemented as soft constraints using the slack variable ϵ. The softened output constraints are written as

$$y_{\min} - \epsilon \leq y_c(k) \leq y_{\max} + \epsilon, \quad k = 1, \ldots, N_p$$

with

$$\epsilon \geq 0.$$

Here, $y_c(k)$ denotes the selected constrained outputs at prediction step k, while $y_{\min}$ and $y_{\max}$ are the corresponding lower and upper output bounds. The stacked output bounds over the prediction horizon are denoted by $\bar{y}_{\min}$ and $\bar{y}_{\max}$. Using the condensed prediction model, these constraints can be stacked across the prediction horizon as

$$\begin{bmatrix} A_y & -\mathbf{1} \\ -A_y & -\mathbf{1} \end{bmatrix} \begin{bmatrix} U_c \\ \epsilon \end{bmatrix} \leq \begin{bmatrix} \bar{y}_{\max} - \bar{C}_y F x_0 \\ -\bar{y}_{\min} + \bar{C}_y F x_0 \end{bmatrix}$$

where

$$A_y = \bar{C}_y \Phi_u$$

and $\mathbf{1}$ denotes a column vector of ones.

DEPARTMENT OF MECHANICS AND MARITIME SCIENCES
CHALMERS UNIVERSITY OF TECHNOLOGY
Gothenburg, Sweden 2026
www.chalmers.se

CHALMERS
UNIVERSITY OF TECHNOLOGY